Digital Flow Visualization Techniques Applicable to Compressible and Incompressible Flows

Thesis

Submitted To

Graduate Engineering & Research
School of Engineering

UNIVERSITY OF DAYTON

In Partial Fulfillment of the Requirements for

The Degree

Master of Science in Aerospace Engineering

by

David S. Bell

UNIVERSITY OF DAYTON

Dayton, Ohio

December 1993

DIGITAL FLOW VISUALIZATION TECHNIQUES APPLICABLE TO COMPRESSIBLE AND INCOMPRESSIBLE FLOWS

Approved by:

Michael Brendel, Ph. D.
Assistant Professor,
Mechanical and Aerospace Engineering
Committee Chairperson

L. Earl Miller, Ph. D.
Associate Professor,
Mechanical and Aerospace Engineering
Committee Member

Thomas Kelly, Ph. D.
Assistant Professor,
Mechanical and Aerospace Engineering
Committee Member

Donald L. Moon, Ph. D.
Interim Associate Dean/Director,
Graduate Engineering and Research

Joseph Lestingi, D. Eng., P.E.
Dean,
School of Engineering

ABSTRACT

An experimental study has been performed to locate flow structures in subsonic, transonic and supersonic flows. The approach involves a laser light sheet with a light scattering tracer directly injected into the flow. Images are captured by a slow-scan digital camera then downloaded to a file that can be enhanced and reproduced. Proof-of-concept tests using natural condensation as the tracer have resulted in images of two dimensional shock waves and related shock-boundary layer interaction about small models in a supersonic flow. The techniques are extended to low subsonic unsteady conditions where acoustically enhanced vortices are shed from a circular cylinder. Phase-locking techniques are also investigated by applying the light sheet to a single blade row rotating at low frequency. The digital camera is successful in capturing the light sheet interaction with a fan blade as provided through an acousto-optic modulator. The goal is to determine the most suitable flow visualization and image processing techniques for use in an operating transonic compressor rotor.

ACKNOWLEDGMENTS

The author acknowledges the tremendous support of Dr. Michael Brendel of the University of Dayton. His insights and patient direction is gratefully appreciated. Also, I am grateful to Mr. Bob French for his assistance in the lab, and to Professor Doug Hanneman for providing some very necessary equipment. Many thanks go out to my wife, Karen, who hasn't lost sight of the light at the end of the tunnel. This work is supported by the United States Air Force, Wright Laboratories Aero Propulsion and Power Directorate, and the University of Dayton Mechanical & Aerospace Engineering Department.

This document was produced on a Packard Bell 486 personal computer and output on a Hewlett-Packard HP Laserjet 4 printer at 600 dpi resolution. Typesetting was done in WordPerfect® 5.2 for Windows™ using TrueType™ Arial and Times New Roman fonts. The digital images were enhanced and annotated using DrawPerfect® 1.1. All other drawings were generated with Professional Draw® 1.0a for Windows™. Color images were printed on a Tektronix Phaser III.

TABLE OF CONTENTS

LIST OF ILLUSTRATIONS

LIST OF TABLES

LIST OF SYMBOLS

D	diameter
h	latent heat
m	molecular weight
$\dot{m}$	mass flow rate
M	Mach number
n	vortex shedding frequency
P_{sat}	water vapor saturation pressure
Re	Reynolds number
S	Strouhal number
T	static temperature
T_b	boiling point temperature
V	velocity
x	humidity ratio
β	shock angle
γ	ratio of specific heats
δ	shock detachment distance
θ	body deflection angle
λ	wavelength

μ	Mach wave angle
φ	relative humidity
∞	freestream condition

CHAPTER

1

INTRODUCTION

1.1 MOTIVATION

The present study is driven by the needs of the turbomachinery community to improve the efficiency of compressor rotors. The pressure ratio and efficiency of the compressor greatly effect the performance of an axial flow engine as a whole. Therefore, it is understood that for all components downstream of the compressor, their effectiveness is largely influenced by the diffusion of the oncoming stream through the blade passages without significant losses. These losses can occur by the existence of shocks about the compressor blades and their interaction with boundary layers. It is necessary, for the advancement in turbomachine design, that the nature and extent of internal flow structures which contribute to inefficiencies be identified.

The identification of flow structures presents a challenge for internal flows. Not only is the high speed rotating machinery a safety risk, the introduction of instrumentation within such confined areas and clearances is difficult. The approach presented here consists of several phases which represent incremental advances toward application to rotating turbomachinery. The marriage of these processes will ultimately be used to visualize the flow in a transonic compressor rotor and identify the shock location and interaction. A digital camera system combined with novel flow illumination techniques

has been developed to acquire images of flow around various bodies. The operation has successfully been applied to an intermittent blow-down facility with supersonic nozzles. Additionally, images have been acquired from a rotating blade row intercepting a pulsed laser light sheet timed at the frequency of rotation. Finally, an attempt is made to capture images of vortex shedding from a circular cylinder in subsonic cross flow. The vortices are revealed by illuminating an artificial smoke tracer.

The situations in which the techniques of this study could be used would seem limitless. Practically, any circumstance where the flow field is of interest and optical access is available would benefit from the visualization methods. Such research might include:

- compressor rotors
- turbines
- wind tunnel testing
- pressure paint
- classical demonstrations
    - flow about elementary bodies such as flat plates, cylinders, wedges, steps.
    - shock tubes

To assist in the illumination of the flow through the blade passages of the transonic compressor rotor, a probe is being designed whereby a laser beam will be directed normal to the flow behind the rotor blades then turned upstream. Near-supersonic flow conditions exist at the hub of the rotor and subsonic flow occurs at the blade tips. The techniques presented should assist in revealing the shocks occurring between the hub and tips and the associated boundary layer interaction.

Suggested methods for these investigation have included laser induced gas fluorescence, holographic interferometry, schlieren or shadowgraph, and laser illuminated flow field techniques.

1.2 Existing Methods

Laser velocimetry is a common approach to map a flowfield with an illuminating particle. This technique as applied to a transonic fan can be found in [1] and [2]. The particles are used to seed a flow and then are illuminated by a laser at locations of interest. A device then optically measures the scattered light of the particles which pass through the region. Post processing of the data results in the mapping of velocity vectors. One deficiency of this method involves the assumption that the particles follow the air particles. However, when the tracer encounters a shock, it is unable to follow velocity discontinuity across the shock. Tests have included corrections to account for the particle lag. In order to map an entire flow field, a large amount of data is usually taken over a long time span and averaged. The long acquisition period requires a steady maintenance of the facility.

Classical methods for imaging shock structures include shadowgraph, schlieren and interferometry. These methods produce images based on density variation in the flowfield which refract light. As applied to rotating hardware at excessive rates, one can imagine the difficulty of lens and mirror alignment. These non-intrusive techniques are essentially impossible for acquiring images between rotor blades.

Similar to the method used in this study, is the technique referred to as laser-induced gas fluorescence (LIF). LIF involves the fluorescing of a seeded particle by striking it with a pulsed laser. Density variations in the flow are revealed by the refraction of the fluorescing particles. A survey of various LIF techniques is presented by Allen, et al. [3]. One of the earliest applications of LIF to a compressor rotor was by Epstein [4].

The location of shock structures impinging on models can be determined through wind tunnel testing. A laser-induced fluorescing particle is mixed in a motor oil matrix and coated on the model. Upon reaching locally sonic speeds, the shock structure origin

is revealed by the coalescing of the seed particle at the point of shock attachment. However, the secondary emission of light from the tracer does not reveal the shock structure elsewhere, such as in a blade passage. Additionally, the test must be interrupted to reapply oil to the surface for further imaging.

It is desirable to use a tracer that is not short lived as is the case of LIF particles. One such seed particle would be water vapor–either ambient or controlled. Rather than providing short bursts of high energy, a laser sheet could continuously reflect off the vapor particle and emit an image to the camera. The light scattering particles could be artificially introduced as well. This was the approach taken by McGregor [5] in a study to determine the humidity required for optimum imaging of the flow about a delta wing.

CHAPTER

2

PHYSICAL CONCERNS

2.1 CONDENSATION EFFECTS

It was Prandtl in 1935, who presented schlieren photos of shock-like formations behind a nozzle throat [6]. In the same paper, Wieselsberger noted that the location of the shock-like structures probably depended on the air humidity [7]. Subsequent investigations into this issue led to the development of air drying equipment for supersonic facilities. It was shown by Eber and Gruenewald [8] that supply air needs to be dried to a humidity ratio (or, mass ratio of water vapor to dry air) of $x=5\times10^{-4}$ for condensation shocks not to occur in a nozzle. Therefore, testing could be achieved nearly humidity free.

In a region of the flowfield where the temperature and pressure are low enough, condensation can occur due to a phase change of one or more of the fluid components. Such is the case where the gas in a nozzle undergoes an expansion to a sufficiently low temperature. This occurs at large Mach number.

From the methods outlined by Wegener and Mack [7], one can determine the relative humidity of a flow and realize its effect on flow quality. Relative humidity of moist air is defined as the ratio of the partial pressure of water vapor to saturated water vapor pressure with respect to the same static temperature and is given by

$$\varphi \equiv \frac{p_v}{p_{sat}} . \tag{1}$$

For a relative humidity of $\varphi>1$, conditions exist for condensation to begin. If $\varphi>1$ and no condensation is present, the flow is said to be *supersaturated.* Conversely, if $\varphi<1$, the flow is prone to evaporation. The temperature at which condensation may begin, (i.e., $\varphi=1$), is referenced as the dewpoint. When the temperature drops below the dewpoint the air is *supercooled.*

From Wegener [9], the water vapor saturation pressure, p_{sat}, is a function of the static temperature, T.

$$\log_{10} p_{sat}(atm) = 6.064 - \frac{2263}{T(K)} \tag{2}$$

The constants in the vapor pressure equation are tabulated by Wegener for various substances.

A relationship derived by Campbell, et al. [10], expresses the local relative humidity as a function of freestream relative humidity and local and freestream values of static pressures and temperatures. The relative humidity equation is then a function of local flow properties.

$$\varphi = \varphi_\infty \frac{p}{p_\infty} 10^{\left[-\frac{2263}{T_\infty}\left(\frac{T/T\infty - 1}{T/T\infty}\right)\right]} \tag{3}$$

Notice that an increase in p and a decrease in T will result in an increase in the local relative humidity, φ; such is the case of an expanding flow in a nozzle. The case of a boundary layer experiencing an increase in temperature next to a body, results in a local

decrease of relative humidity. Wegener and Mack showed that a shear flow is a way to revert condensate back to a vapor.

As seen in equation (3), φ has a linear dependence on local pressure, while having a $\log_{10}$ dependence on local temperature. This suggests that local temperature changes have a greater influence on local relative humidity than comparable changes in pressure. Therefore, a large temperature rise across a shock drives the humidity down although a large pressure rise is also occurring. So what is likely to occur about a transonic compressor rotor is an expansion of the flow over the curved blade causing a visible condensation region. As the flow leaves the rear of the blade, the temperature rise across a recompression shock may evaporate the condensation that was formed upstream. A example of this phenomenon presented by Campbell shows an F-14 aircraft generating an enormous condensation pattern during level flight in the transonic regime.

Since the saturation pressure, p_{sat}, is a function of static temperature from (2), and since T is a function of local Mach number, then we reason that φ is a function of M, moisture content, temperature, and pressure in a nozzle supply section. Not considering the presence of a boundary layer, if expansion of vapor occurs in a properly designed nozzle, the entropy will remain constant until condensation take place. Hence, with an entropy rise due to condensation effects, the flow quality will be driven below that of design. The process of condensate formation is one in which latent heat is released to the flow.

The system can be expressed through a Mollier diagram (or, enthalpy versus entropy). The locus of points, called a *Rayleigh* curve, can represent subsonic to supersonic conditions based on the heat added to or removed from the system. Obviously, while traversing from subsonic to supersonic extremes, the curve must pass through the sonic point—this is the point of maximum entropy. The nature of a Rayleigh curve suggests that if initial conditions are subsonic, the addition of heat will drive the system

towards the sonic point. Similarly, supersonic initial conditions result in the system being driven to sonic flow as heat is added. The Rayleigh curve in our interest represents the process of traveling from initial conditions of the supersonic nozzle to some point downstream of the nozzle throat. Each point on the curve reflects a value of heat, q, added or removed from the system. Recall from the energy equation that q is a function of change in total temperature and the specific heat at constant pressure, c_p.

$$q = c_p\left(T_{o2} - T_{o1}\right) \tag{4}$$

Therefore, as condensation releases heat to the flow, the total temperature will rise and the Mach number will decrease.

2.2 TRACER PROPERTIES

McGregor [9], based on his vapor-sheet study, compiled a list of desirable properties for an artificial seeding medium. The fluid should be:

- non-corrosive to the equipment
- commercially available
- chemically stable
- low toxicity
- nonflammable
- high molecular weight
- possess a saturated vapor density such that
  - a sufficient amount can be injected before reaching saturation under stagnation conditions
  - an excessive amount is not required to produce saturation at the working section static temperature.

The latent heat, h, and molecular weight, m, are related by Trouton's Rule, $hm=CT_b$, where C is a constant (=21) and T_b is the boiling point of the fluid. As a consequence, a high molecular weight corresponds to a low latent heat of evaporation.

For the follow-on transonic application, it is proposed that a fluid be used with the properties mentioned above. An artificial smoke generator, is investigated that uses a proprietary fluid. The fluid has a glycol base of one or more of the following fluids: propylene glycol, triethylene glycol, and/or polyethylene glycol. Polyethylene glycol has a molecular weight in the range of 380-420 while water's molecular weight is 18. McGregor used carbon tetrachloride in his vapor-screen experiments and it has a molecular weight of 154. The glycols above have been rated with very low toxicity. The vapor densities of the glycols are as high as 5.18, relative to water vapor density being 1.0. A discussion of the fog generator is presented in Chapter 5.

For many supersonic studies, the humidity effects in a nozzle are avoided by using an inline dryer. For the supersonic phase of the present study, however, the existence of natural occurring water vapor will be exploited to visualize shocks.

CHAPTER

3

SUPERSONIC DEMONSTRATION

3.1 INTRODUCTION

As a demonstration of the proposed imaging techniques, a blowdown facility was used to exhaust compressed air through a nozzle. The air jet was accelerated through a supersonic nozzle then impinged upon a model to generate shock structures. A schematic of the apparatus can be seen in Figure 1. The resulting shock waves were captured with a high speed digital camera and subsequently stored on a computer. The images are of such quality that the features of the shock structure are identifiable—similarly, classical shock-boundary layer interactions can be captured.

3.2 EXPERIMENTAL EQUIPMENT AND FACILITIES

3.2.1 BLOWDOWN FACILITY

The UD supersonic blowdown facility [11] in Figure 2 provided the flow for initial applications of the visualization techniques. Its free jet characteristic has several inherent advantages over enclosed indraft or closed loop tunnels. Besides easy access to the model (no enclosed test section), there is no choking problem caused by an oversized model in the test section. Additionally, starting and running compression ratios are similar, since no 'overpressure' is required to start the flow [12]. Unfortunately, the lack of a

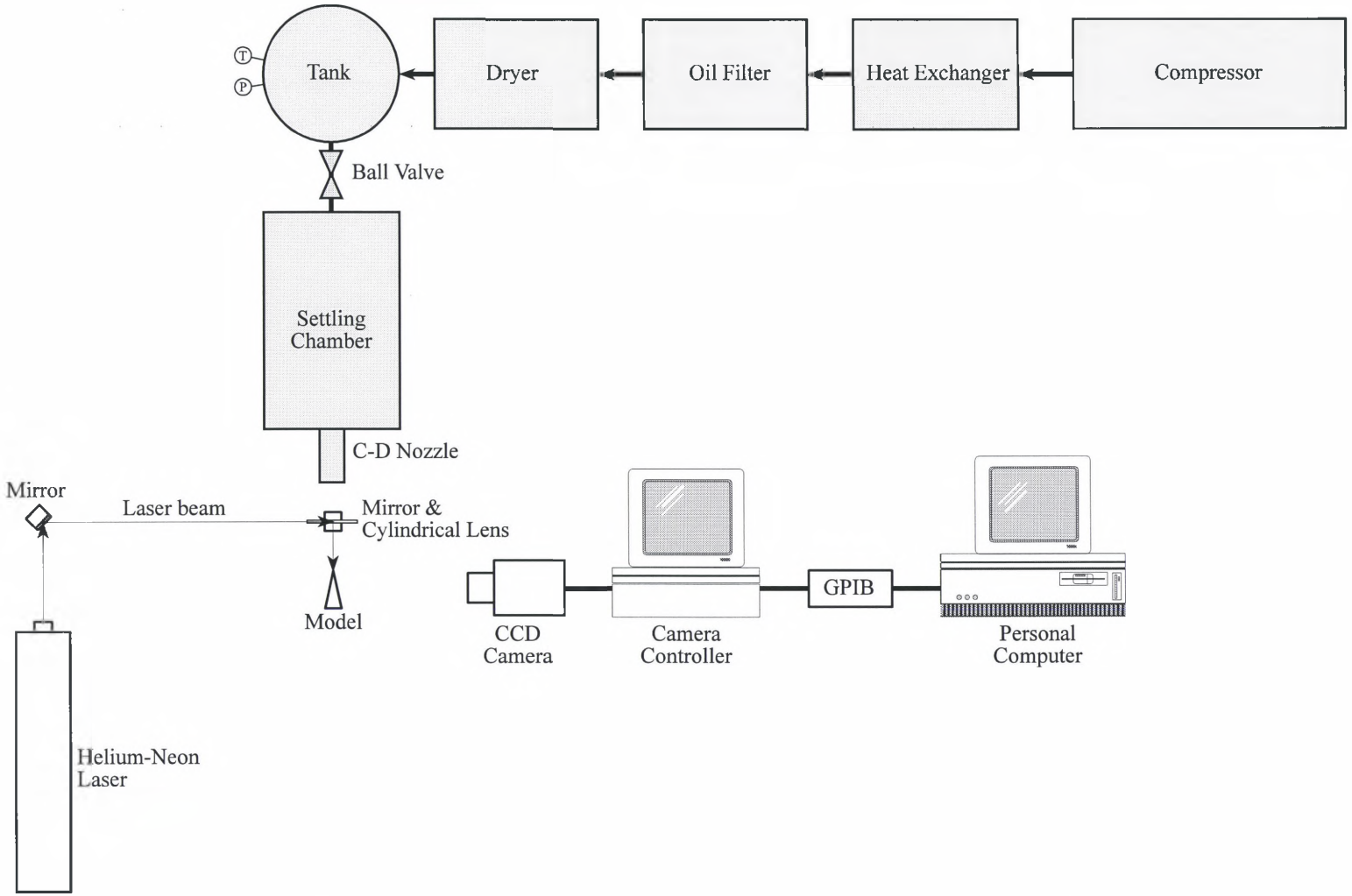

Figure 1: Schematic of supersonic facility and experimental setup.

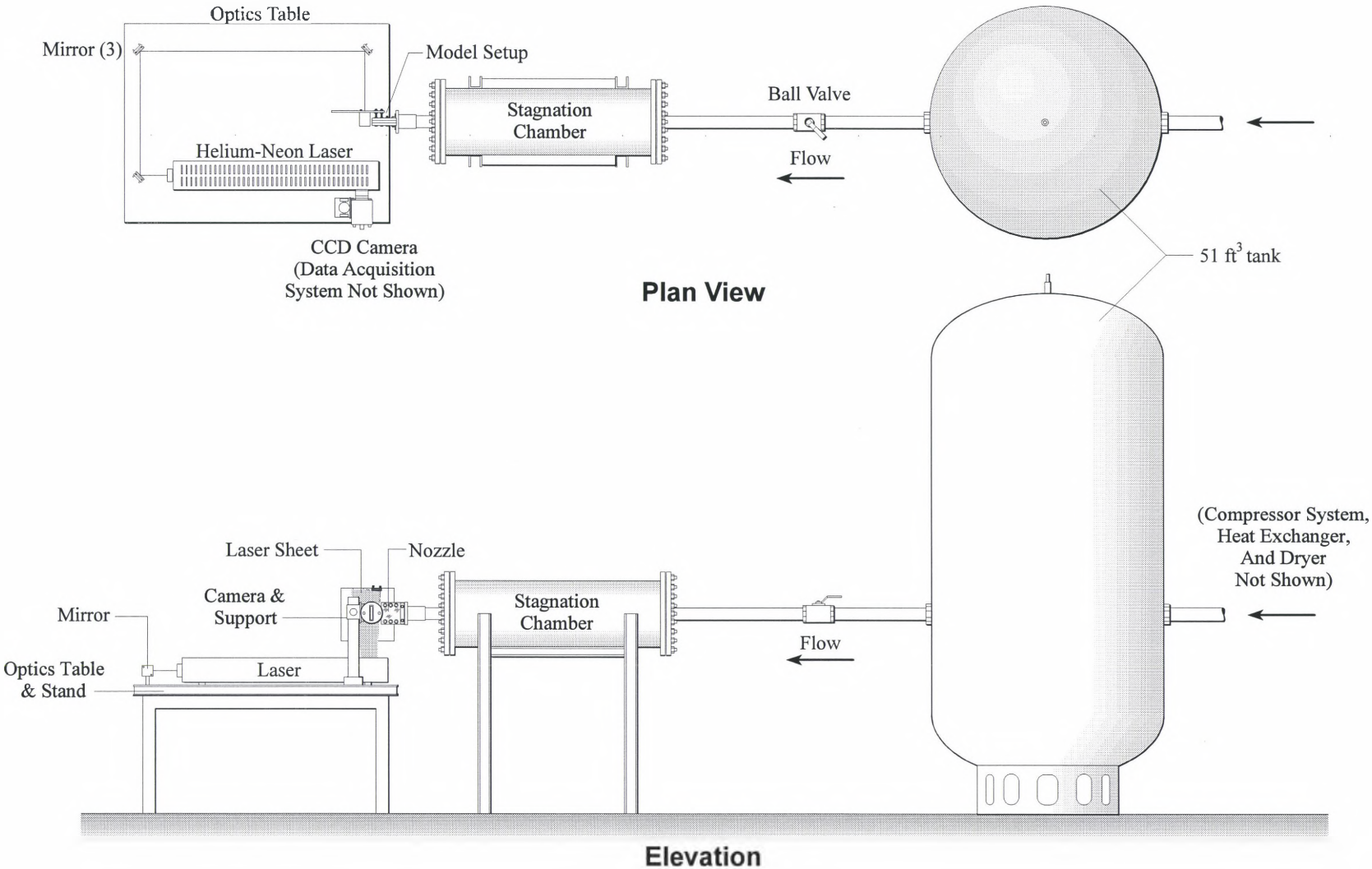

Figure 2: Supersonic blowdown facility.

controlled test section allows for unbearable noise levels from the jet. An Ingersoll-Rand 15 HP (11.2 kW) three-cylinder compressor generated 51 ft^3 (1.44 m^3) of compressed ambient air to fill a double-walled Kargard Industries tank. The working pressure of the tank is rated at 208 lb/in^2 (1.43 MPa) and the temperature rating is 450°F (910°R, 505 K). A maximum pressure used in the experiments described below was in the range of 180-200 lb/in^2 (1.24-1.38 MPa). The tank is equipped with a safety valve to prevent overpressure. The temperature and pressure were monitored by a bourdon-tube pressure gauge and a J-type thermocouple attached to the tank. The only considerable source of heat addition to the tank was that due to the heat of compression. Before entering the tank, the air passed through a water cooled counter-flow heat exchanger to remove the heat of compression and to condense vaporized compressor oil. An in-line filter is available to remove this oil if present. Downstream of the heat exchanger and filter is an Ingersoll-Rand Hydrobloc dryer to remove moisture in the flow. Since the procedure was to utilize the ambient water vapor, the dryer was not activated.

All piping downstream of the pressure tank is 2 in (5.08 cm) diameter cast iron and has a ball valve in-line between the tank and the stagnation chamber. The flow proceeded downstream through a 1.2 ft^3 (0.034 m^3) cast iron stagnation chamber. The stagnation (or settling) chamber ensures high quality flow by reducing turbulence placed in the stream through the ball valve and piping. However, as flows in wind tunnels approach transonic and supersonic speeds, turbulence is less of a concern to the flow. Due to locally lower velocities, the stagnation chamber exhibits higher static pressures than at any point downstream, yet considerably lower than the storage tank [12].

3.2.2 NOZZLES

While the initial study will eventually lead to transonic applications, two supersonic nozzles were used for the purpose of creating shocks. The nozzles were

designed to produced 1.5 and 2.0 Mach numbers. The diverging section of the nozzles were designed using the method-of-characteristics for minimum length nozzles—a method found in many compressible flow texts. The nozzles are attached to the exit end of the stagnation chamber with a short cast iron pipe nipple. Quick change-out of the nozzle was made possible with this fixture. Inside the short cast iron pipe are 3:1 elliptically contoured slugs to contract the flow smoothly prior to entering the nozzle. The contraction allowed the flow to transition from the 2 in (5.08 cm) diameter pipe to a nozzle inlet area having dimensions of 2 in × 0.5 in (5.08 cm × 1.27 cm). Each nozzle was fabricated with a sandwich construction of three 0.5 in thick acrylic sheets. The center sheet is cut to provide the upper and lower contour of the nozzle while the two outside sheets provided the sidewalls for a 2-D effect. The converging section was fashioned with a circular arc profile leading to a throat section of 1 in × 0.5 in (2.54 cm × 1.27 cm). The exit heights of the nozzles are 1.2 in (30 mm) and 1.7 in (43 mm) for the Mach 1.5 and Mach 2.0 nozzles, respectively. An exit view showing the general shape and fabrication of a nozzle can be seen in Figure 3. The design velocity (V) for each nozzle, the associated Reynolds numbers (Re) for each model, and the mass flow rates ($\dot{m}$) are shown in Table 1 based on theoretical calculations. The calculations assume calorically perfect gas (γ=1.4) and an ambient temperature of 80°F (300 K or 540°R). The model geometries are discussed in Section 3.4.

Table 1: Nozzle/model velocities and Reynolds numbers.

	M = 1.5 V = 1458 ft/s $\dot{m}$ = 0.44 lb_m/s	**M = 2.0** V = 1744 ft/s $\dot{m}$ = 0.75 lb_m/s
Wedge	Re = 1.37×10^6	Re = 1.63×10^6
Cylinder	Re = 84,914	Re = 101,570

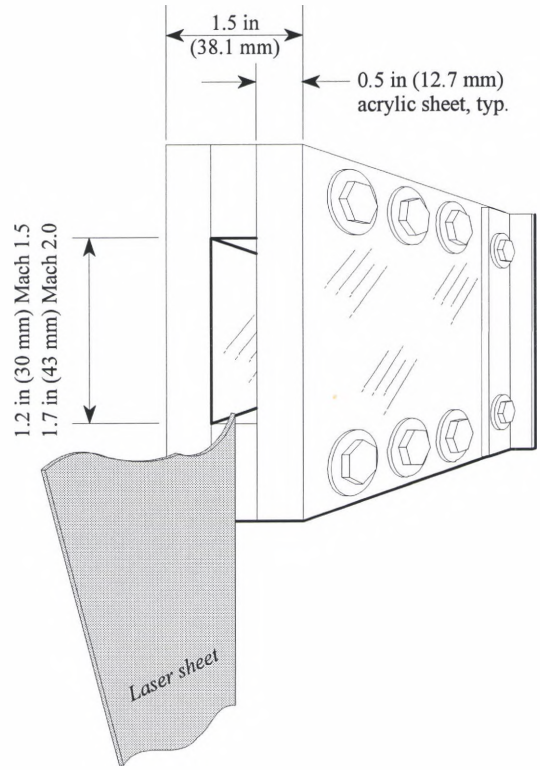

Figure 3: Typical end perspective of nozzle.

A plate was then mounted to the backside of each nozzle (Figure 4). This plate served two purposes: (1) it was a surface to attach black felt for minimizing light reflection and act as a dark background for the images, and (2) it acted as a rigid support for mounting the models. The plate was adjustable along the flow axis to accommodate the displacement of the models from the exit of the nozzle. A sufficient stand-off distance was allowed between the plate and the flow expansion so as not to interfere with the region of interest. A laser light sheet, which is discussed in Section 3.2.4, was directed from below the model and cast a shadow in the upper region of the image. A small mirror was placed at the top of the mounting plate to reflect the incident laser sheet

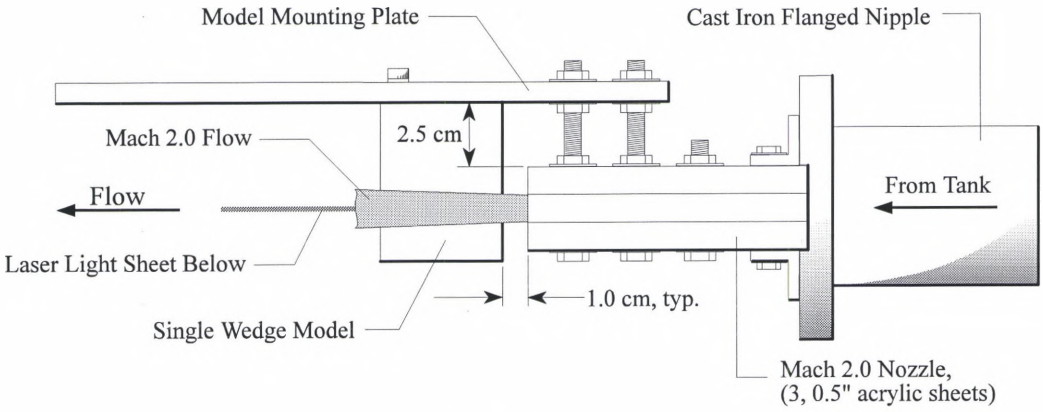

Plan View

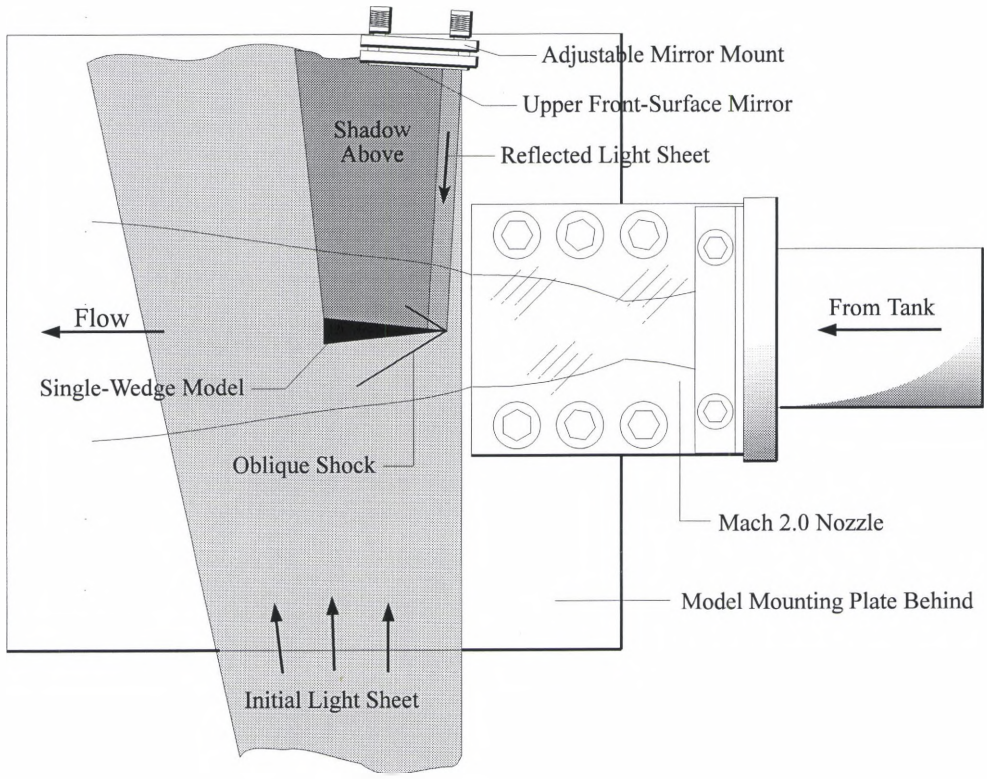

Elevation

Figure 4: Mounting plate and nozzle detail.

and illuminate the initial portion of the body and its associated flow.

Realize that while these nozzles were designed for isentropic conditions, we should expect something less than the design Mach number. The method of characteristics is a technique often used in determining the internal contours of supersonic nozzles beyond the throat. It allows one to define the properties of the flow in the presence of, in our case, the nozzle boundaries. The calculations are generally based on a constant entropy flow, i.e., no shock waves in the design portion of the flow. The converging section of the C-D nozzle is subsonic and accelerates the flow to sonic speed at the throat. Although the viscous effects tend to thicken the boundary layer, it is generally neglected in the converging section without serious consequences [12]. Since the method of characteristics makes calculations resulting in many straight sections to form the diverging section of the nozzle, corrections are usually made for boundary layer effects. No adjustments for the boundary layer were made for the nozzles in the present study. So considering the effect on property ratios and the input of heat to the flow due to the condensing of water vapor, this results in an actual Mach number below the design Mach number. Image analysis in later sections indicates this is so and supports the Rayleigh curve explanation.

3.2.3 MODELS

A library of images was developed in the supersonic case by observing the interaction of two different models with the flow (Figure 5). One was a single-wedge with a 5.8° half-angle and a chord length of 1.9 in (48.26 mm). A very sharp leading edge was ground on the wedge to produce a clean oblique shock. The other model was a small right-circular-cylinder with a diameter of about 3.0 mm. The blunt cylinder was used to generate a bow shock. Both the wedge and cylinder produced shock phenomena that was consistent and very repeatable. To minimize reflections into the camera, the models, which were made of a steel alloy, were painted black.

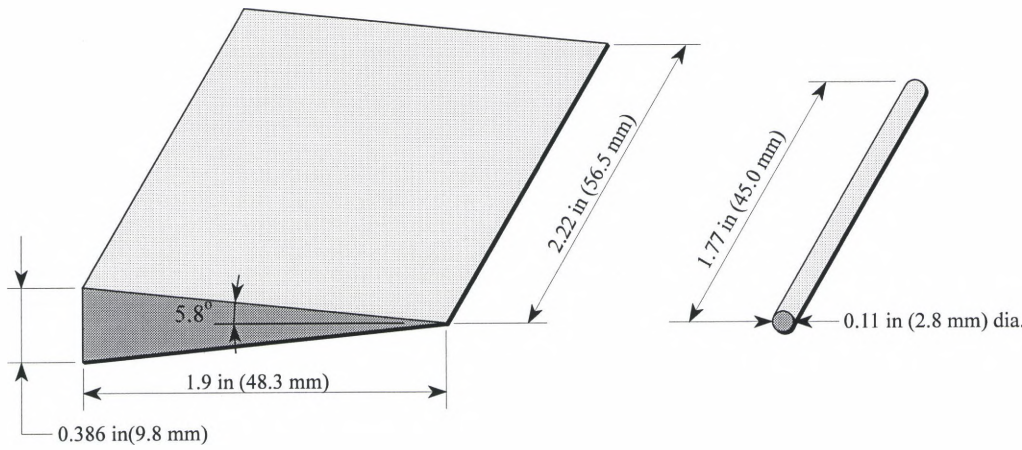

Figure 5: Model geometries for supersonic demonstration.

3.2.4 ILLUMINATION

The lighting was provided by a Spectra-Physics 35 mW Helium-Neon laser with a beam diameter of about 1.25 mm and a wavelength of λ=632.8 nm, which corresponds to orange-red light. The beam divergence is rated at 0.66 mrad. The laser is designed to operate in an environment of 10-50°C (50-122°F) and 10-90% relative humidity (noncondensing).

Upon exiting through the laser mounting bezel, a series of front-surface mirrors guided the laser beam around an optics table to a point below the fluid flow. As Figure 2 shows, a 45° front-surface mirror placed about 35 cm (14 in) below the nozzle centerline directed the beam vertically. Prior to passing through the supersonic flow, the beam was transformed into a sheet of light by passing it through a 5 mm diameter glass cylinder. By fanning out the beam into a sheet we were able to capture a *visual slice of the flow* about the body of interest. The alignment of the sheet was coincident with the vertical centerline of the nozzle exit (Figure 3). For a laser beam of about 1.25 mm

passing through a glass cylinder of 5 mm in diameter, a full divergence angle of about 20° was achieved.

3.2.5 Imaging System

At the heart of the setup is a stand-alone 12-bit digital camera system. All images were obtained by a Photometrics STAR I digital camera with a 50 mm Nikon AF lens. The camera head encloses a scientific-grade CCD (*charge-coupled device*) that initially records an image. A CCD imager is a metal-oxide-semiconductor (MOS) optical detector that is composed of a large number of independent sites where photon-induced charge is stored. When the shutter is activated, the 576 × 384 matrix of 23-micron-square sites, or pixels (*picture elements*), stores a photon-induced charge proportional to the illumination pattern. Its highly linear response provides a performance for quantitative applications even in very low light levels. The intensity data is converted into digital information by a 12-bit analog-to-digital converter with a charge transfer efficiency (CTE) from the array to an output amplifier of 0.999, where 1.0 is ideal.

One important feature of the CCD camera system is the liquid circulation unit. Its has the ability to thermoelectrically cool the camera head to a constant -45°C with an ethylene glycol and water mixture. The need to cool the camera head is due to photon interaction with the CCD array. The cooling action is essential to greater light sensitivity and better performance.

The digitizing and storing of the gray-scale image is done through the camera controller which also handles the video display functions. Although packaged routines exist for transfer of the data to a file format, the one used here was developed at UD [13]. Data was transmitted to a PC via the camera controller's IEEE-488 communications port and the PC's GPIB (*General Purpose Interface Bus*) then stored it in a TIFF (*Tagged Image File Format*) file. The image in the TIFF format can be read in by many image

processing programs, including word processors, desktop publishing packages and other graphics programs.

3.3 Data Acquisition and Processing

It was shown earlier in Figure 2, the general layout of the optical equipment, laser, and model relative to the nozzle and flow. The camera was positioned about 18 in (457 mm) from the vertical plane of the nozzle. The camera axis was aligned normal to the light sheet and coincident with the leading edge of the model. If done correctly this would minimize light reflections from the models and nozzles, and reduce parallax or 3-d effects in the images. To properly scale the images, a reference grid was placed in the plane of the light sheet and recorded. This resulted in an image resolution of about 152 pixels/in (6 pixels/mm) using the 50 mm lens.

While the tank was being pressurized to about 200 lb/in^2 (1.38 MPa), the optics and camera system were readied to acquire an image. The ball-valve was manually opened and an image was obtained when the condensing vapor in the flow revealed a significant flow structure about the model. In most instances the process of opening the valve and imaging was done in 5 to 7 seconds. A typical run resulted in a tank total pressure drop to about 150 lb/in^2 (1.03 MPa) and total temperature drop to 0°F (273 K or 460°R). A dense 'cloud' similar to a rolling morning fog continued to slowly spill out of the nozzle after the valve was closed. As the tank was being repressurized for the next test, the current image was analyzed on the camera video monitor for any necessary modifications of the setup or camera adjustments.

The UD supersonic blowdown facility was constructed without a light-tight enclosure. Since the facility is intended to be used for other applications, it was not feasible to fabricate an enclosure around the high-speed flow equipment. To control all light sources such that the laser beam was the primary source, all testing was conducted

at night. However, some foreign light was still present from outside lights and the laser plasma tube. This did not present any problems for acquiring the images. In fact, the undesirable light tested the ability of the camera system to acquire usable images in less than ideal lighting conditions.

The digital camera has a 12-bit dynamic range equating to an intensity resolution of 4096 shades of gray. However, most acceptable images of the supersonic flow had a dynamic range of 8-bits (256 gray levels). Each image was analyzed on a VGA monitor having 4-bit dynamic range or 16 gray levels. For the images having a full 8-bit range, therefore, isolation of a particular region of the image was possible at the expense of blackout or saturation elsewhere. Software was written in-house to accommodate the enhancement of details. Once the dynamic range of the individual image was determined, it was converted to an 8-bit file primarily to save file storage space. It was this file that was eventually reproduced on a 600 dpi laser printer. As will be seen later, details such as oblique and bow shock waves, separation bubbles, Mach waves, and expansion regions were ascertainable.

3.4 Results

Through several sessions, a single-wedge and circular cylinder were placed in the supersonic flow generated by Mach 1.5 and 2.0 nozzles. One of the constraints of the method of characteristics is that the nozzle design is for inviscid (isentropic) flow. Since in the real world viscosity, mass diffusion, and thermal conduction exist, one should expect less than ideal performance due to boundary layer formation and heating due to the condensation process. It is estimated that a Mach number efficiency of about 90% was achieved relative to nozzle design Mach number.

Many images were recorded during the supersonic runs and some of the best are presented, covering all Mach number/model configurations. Typically, the exposure time

was a tenth of a second (0.1 s) which is the lowest setting the camera controller will allow. With the camera positioned a distance of about 18 in (457 mm) from the flow, the entire body and surrounding flow phenomena were recorded. The field of view in most cases was approximately 3.8 in × 2.5 in (96 mm × 64 mm). The lens aperture was generally set between f/4 and f/8.

The glass cylinder used to spread the laser beam into a sheet was not of optical quality material, therefore was less homogeneous than an optical lens. The only noticeable effect was the existence of light striations running top to bottom in most of the images.

The approach taken so far has been obtaining planar images by using condensing water vapor that simply existed naturally in the room. Since this natural condensation was proven adequate in scattering light, it was the only tracer used. From the discussion of condensation effects on nozzles in Chapter 2, it is arguable that condensation shocks could have been taking place during the tests runs of this study.

3.4.1 Right-Circular Cylinder

Figure 6 shows a strong bow shock fully developed ahead of a 0.12 in (3 mm) diameter cylinder using the Mach 1.5 nozzle. The image is printed at a slightly larger scale, so a scale factor of 1.8 should be used for all calculations made directly from the image. The cylinder, which is normal to the page, was placed 0.28 in (7 mm) from the exit of the nozzle. Above and below the cylinder are dark stripes. These are the shadows off the cylinder caused by the incident light sheet and the reflected sheet from the upper mirror (not shown). Evident in all the images are the light and dark areas. The lighter areas indicate a density concentration whereas the darker areas around flow structures represent a decrease in density. Faintly visible are a pair of Mach lines, or infinitely weak oblique shocks, merging just outside the nozzle exit and appear to be located off-axis.

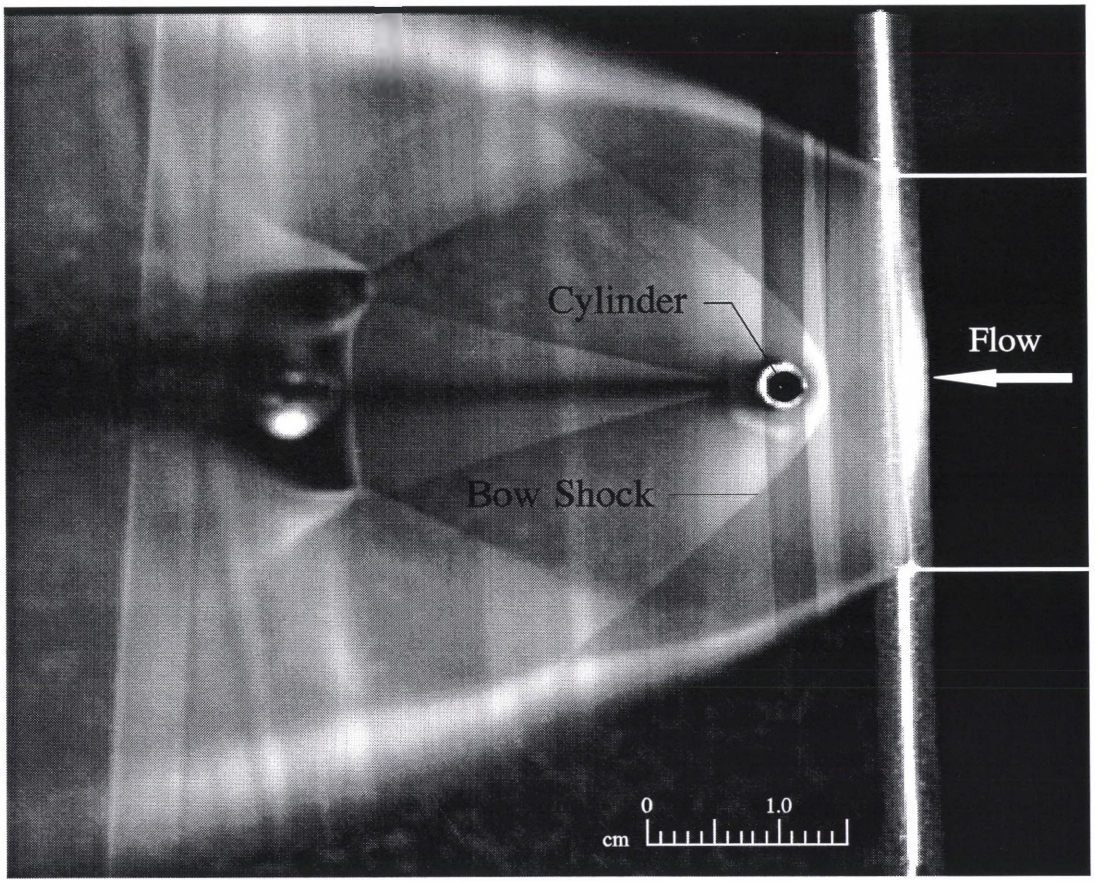

Figure 6: Mach 1.5 flow about a 3 mm diameter cylinder normal to the flow. (Scale: 1.75x)

Since one would expect symmetry from an ideal nozzle, the off-axis problem could be attributed to inconsistencies in the nozzle fabrication and alignment. Noticeable on the upper and lower edges of the nozzle exit, are the formations of shear layers. The underexpanded flow leaving the nozzle is surrounded by still air and produces a turbulent mixing zone for a pressure boundary. Similarly, the constant ambient pressure provides a boundary condition.

A detachment distance, δ, of the bow shock relative to the leading edge of the cylinder can be calculated to be approximately 0.083 in (2.1 mm). At centerline of the body and flow interaction, the upstream flow is normal to the wave and corresponds to a normal shock locally. Following along the shock a point is reached where a streamline experiences the maximum deflection relative to centerline. This represents the dividing line between a strong and weak shock. Slightly beyond this point the flow becomes sonic behind the shock thus enveloping a subsonic region between it and centerline. The flowfield, shock detachment distance, and shape of the shock are driven by the upstream Mach number and the shape of the body. In the last three decades, time-marching numerical techniques have been developed to sufficiently solve the non-trivial blunt body problem. Although application of these techniques could have been applied here to back-out the true upstream Mach number, a simpler approximate approach was used. From oblique shock theory, an upstream Mach number can be determined from $\mu=\sin^{-1}(1/M)$, where μ is the Mach wave angle relative to the flow axis. Using this estimation, the Mach lines at the Mach 1.5 nozzle exit reflect an average Mach number of about 1.35. This is a 90% efficiency for nozzle referencing design Mach number. Since the cylinder is very close to the Mach line intersection, and assuming that little expansion has taken place in this short distance, it is reasonable to say that about a 1.35 Mach number is ahead of the bow shock at centerline. Considering a normal shock at the bow shock centerline, a look-up in a normal shock table says that the flow immediately downstream of the

normal portion of the bow shock is M≈0.76. This supports the explanation of the subsonic envelope discussed above.

Downstream of the cylinder about 3 cm, it is apparent that a bolt is in view. This was placed there to fill the mounting hole vacated by the removal of the wedge model, and to help keep the black cloth attached to the rear mounting plate. It is believed to have no effect on the flow, since no flow phenomena (i.e., shocks) are generated from its existence and since it is behind the general plane of the flow. At first glance, the complex shock structure downstream of the cylinder may appear to be interference with the back mounting plate. However, it is pointed out by Pope and Goin [12] that this is simply a 'second throat' effect. When two oblique shocks converge, as in the case of the upper and lower reflected shocks, they essentially act as converging 'boundaries' to a throat area. The vertical white line that looks like a density concentration is just that—a normal shock migrating to a point such that the flow is choked between the two reflected shocks. It is also possible for the free jet static pressure to be below ambient. The pressure aft of the normal shock is below ambient and the normal shock remains. Notice that the cylinder is slightly below centerline of the nozzle. This may explain the smaller normal shock existing above the bolt. It is formed at the convergence of the upper reflected shock and the wake recompression shock behind the cylinder and represents another locally choked flow. Reduced mass flow in the choked flow is indicated by the darker regions downstream of the normal shocks. It will be seen later that a similar normal shock also persists about the wedge in a supersonic flow due to the same phenomenon.

A Mach 2.0 flow over a 0.12 in (3.0 mm) diameter cylinder is shown in Figure 7 inside the right edge of the image and is bright white due to the reflection of laser light off the acrylic material of the nozzle. The cylinder was placed adjacent to the nozzle exit and normal to the flow. Again the flow is underexpanded as evidenced by the slightly

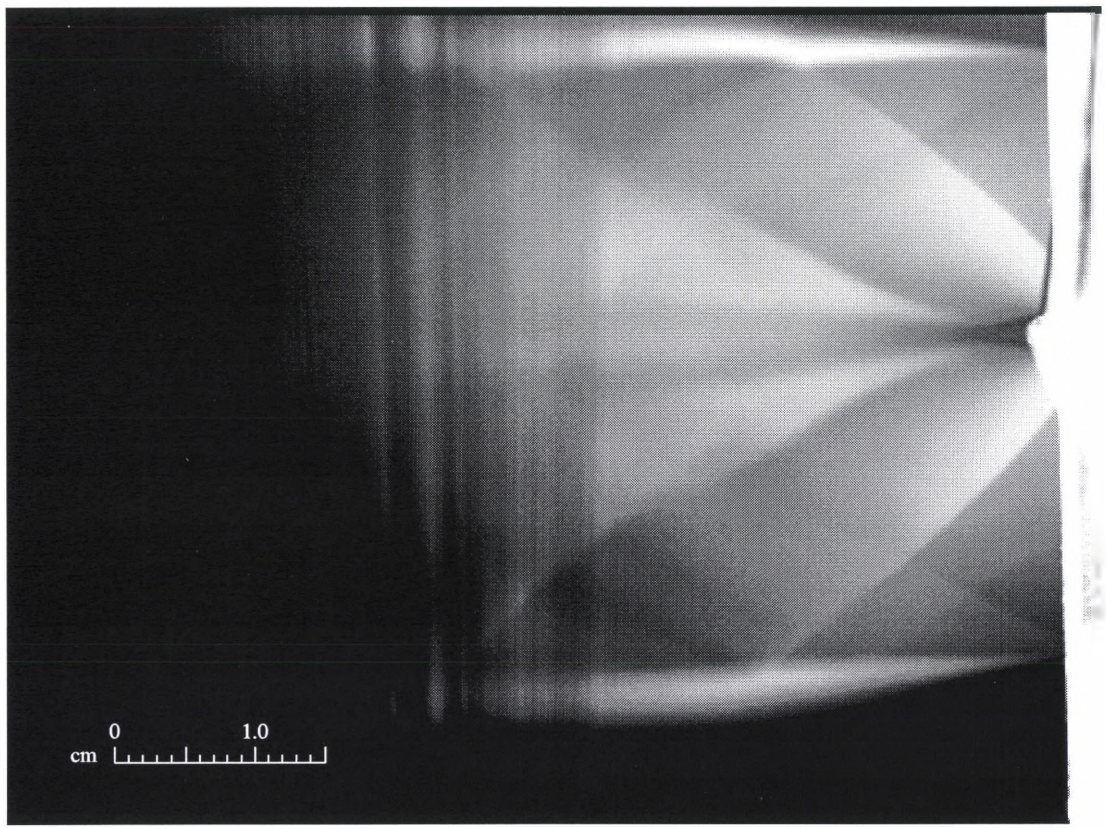

Figure 7: Mach 2.0 flow about a 3 mm diameter cylinder normal to the flow. (Scale: 1.85x)

diverging shear layers on both sides of the nozzle. The bow shock, wake recompression shock, and shear layers are visible also as brighter white. On a gray-level scale the white colors represent regions of higher density such as the nozzle material and condensate in the flow. Notice that the bow shock dissipates from its strongest point at centerline and tends toward weaker Mach waves as it approaches the shear layers. As done in Figure 6, the Mach number can be reasonably determined from the weak Mach waves emanating from the corners of the nozzle. If the 'earliest' visible Mach line is used, calculations reveal a local Mach number of 1.9. Keep in mind that the three-dimensional flow will have a relaxing effect on the shock angles and perhaps contributes to the rate of curvature of the main bow shock as it gets farther downstream. Also evident is a slight bend in the bow shock as it encounters the reflected shocks from the corners of the nozzle. Immediately behind the cylinder is a local decrease in mass (condensate) flow as evidenced by the black region, i.e. lower density. Further downstream the lighter shade of gray reveals the entrainment of condensation.

Two important points are made clear by Anderson [14] regarding the distinction between strong and weak interactions with a free jet and those interacting with a solid boundary:

CASE (i) "Waves incident on a *solid boundary* reflect in like manner, i.e., a compression wave reflects as a compression and an expansion wave reflects as an expansion."

CASE (ii) "Waves incident on a *free boundary* reflect in opposite manner, i.e., a compression wave reflects as an expansion and an expansion wave reflects as a compression."

Viewing Figure 7 the fact that a weak Mach wave is originating from within the solid nozzle, suggest that from CASE (i) it is the result of an incident Mach wave further inside

the nozzle. Proof of CASE (ii) can be seen as the strong bow shock reflects off the free jet boundary as an expansion wave.

The gray scale images provide clear detail of many features. But it was of interest to output color images to see if the detail could be enhanced. A public domain program called *IMAGE* [15] was used for this purpose. This software, which only exists in a Macintosh version, allows the user to perform digital image processing and analysis. Many familiar functions can be utilized, such as display, edit, enhance and print. Additionally, the user can create animations, analyze geometric and mass properties, apply pseudocolor, and interface with appropriate hardware. *IMAGE* was used in this study for its pseudocolor feature. The program has the ability to import TIFF, PICT, and various other common file formats. Several TIFF images were imported to the program, then pseudocolor was applied from a choice of color palettes. Although up to 256 colors can be used, 32 were applied to the color images below.

Figure 8 is the same image shown in Figure 7 but with the application of pseudocolor. Evident in this image is one advantage of color over the gray scale. Since our eyes are accustomed to distinguishing depth, contrast, and brightness with color, it is easier to locate similar regions of light intensity (or fluid density) in the image than with simple gray-scale. Certainly, both color and gray-scale have their merit, but overall one can get a better feel of the flow/body interactions with the color image. Greater contrast is achieved in the case of the near-parallel Mach waves interacting with the nozzle corners and shear layers. Another point to consider is that Figure 7 was laser printed at a resolution of 600 dots per inch (*dpi*) on a Hewlett Packard HP 4, and Figure 8 was printed at 400 dpi on a Tektronix Phaser III. Obviously, other than improving image quality with color, the ability to analyze a hard copy will be output-device dependent.

A scale has been placed on all of the color images with the color intensity corresponding to the gray-scale dynamic range. The lighter colors reflect a more

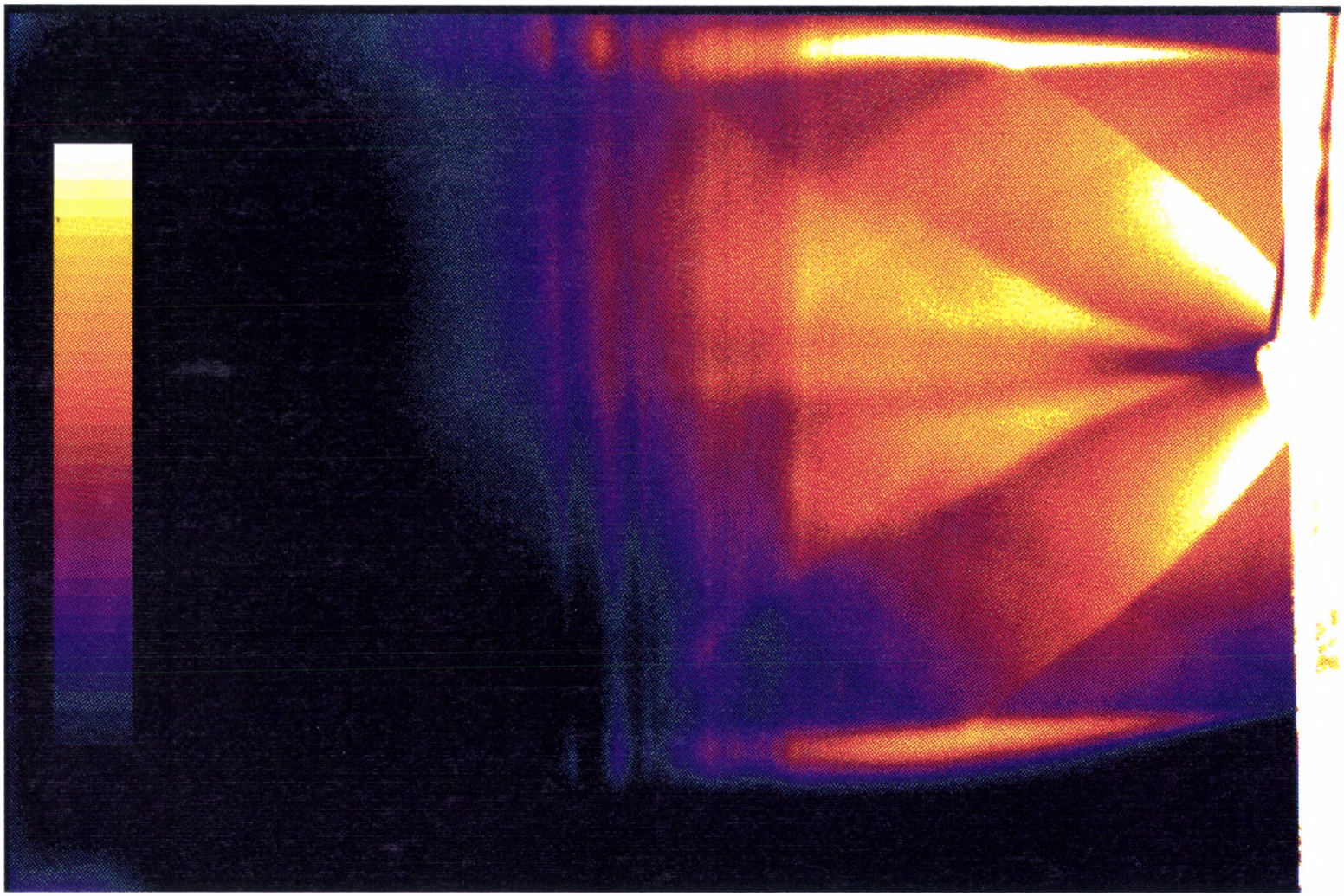

Figure 8: Pseudocolor version of Mach 2.0 image shown in Figure 7. (Scale: 2.32x)

luminous region and visa versa for the darker colors. Caution should be taken when viewing the image. When referencing the local light intensity, one should keep in mind that this assumes a uniform light sheet is entering the flow of interest. This point is illustrated by the vertical light striations—a region of the flow where an obvious nonuniformity of light is occurring. Thus, where fluid density calculations or light intensities are to be analyzed, flow structures could be misrepresented by these aberrations.

3.4.2 SINGLE-WEDGE

In the last section, a cylinder in Mach 1.5 and 2.0 flows was presented. Now we will focus on the same flows about a single-wedge. Evident in images involving the wedge is an oblique shock emanating from the leading edge, but with some curvature. If the edge was indeed razor sharp, shock theory says one should expect a true oblique shock. Upon inspection of the wedge after several supersonic runs, a very slight roundedness was apparent on the lower surface for a distance of about 0.02 in (0.5 mm) from the leading edge. This proved to be a good lesson in how slight imperfections can cause very unexpected results in supersonic flow.

Figure 9 shows a wedge with a half-angle of 5.8° placed 0.38 in (9.7 mm) behind the Mach 1.5 nozzle. The large black area above is the shadow of the wedge due to the incident laser sheet originating from below. A portion of the flow over the upper surface was illuminated by placing a small mirror above to reflect the original light sheet downward. Upon exiting the nozzle, the flow turns outward from the longitudinal axis about 26° to further expand, as can be seen by the diverging shear layers. As in the case of the bow shock from the cylinder, weak Mach waves are visible between the wedge and the nozzle. Again applying shock-expansion theory, the Mach line angles of about 48° suggest that the true Mach number is on the order of 1.3. It would be appropriate to

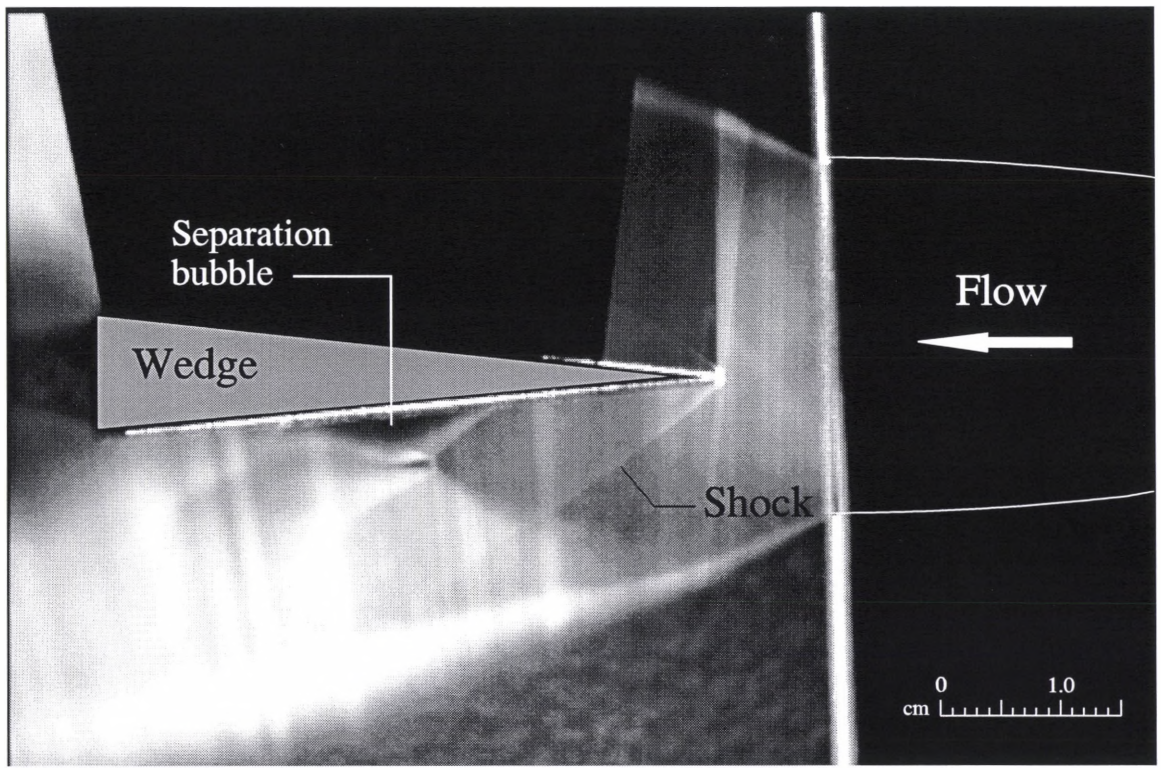

Figure 9: Mach 1.5 flow over a single wedge with a 5.8° half-angle. Note the shock induced separation on the underside of the wedge. (Scale: 1.6x)

check the angles of the oblique shock that lies downstream of these expansion waves. Measuring a shock angle of about 37° and consulting a shock-deflection angle chart (or, θ-β-M chart), we find that the flow just in front of the wedge is about Mach 1.9. The higher Mach number just in front of the wedge can be accounted for by the placement of the wedge in a region of expansion and its associated decrease in static pressure. Hence, a region of higher velocity will occur.

A pseudocolored version of the Mach 1.5 flow over the wedge can be seen in Figure 10. The Mach waves located at the center of the nozzle exit are slightly more noticeable. Likewise, the expansion zone of the flow downstream of the nozzle is much more contrasted in the color image. However, in the color conversion the upper shear layer was deintensified.

A very important flow feature was captured by the camera. The phenomenon is a strong shock-boundary layer interaction and consequential separated flow. Although the complex flow field of this structure has been explained only recently through the use of computational fluid dynamics, the general features are readily explainable. The details can be seen in Figures 11 and 12. An incident shock originating at the shear layer strikes the boundary layer. The adverse pressure gradient across the shock prohibits the boundary layer from continuing in the same path and subsequently the boundary layer separates from the wedge surface. The back pressure is sensed farther upstream through the subsonic region of the boundary layer. To negotiate the newly formed bump in the boundary layer, Mach waves coalesce to form another shock wave. At some point downstream the expanding flow forces the boundary layer to reattach itself and thereby forming another corner to turn. Hence, another oblique shock wave is formed. Due to the severity of separation shown in Figure 11 it is believed to have been an initially laminar boundary layer, which is easier to separate than a turbulent one. The net effect is substantial thickening of the boundary layer with it most likely turning turbulent. A

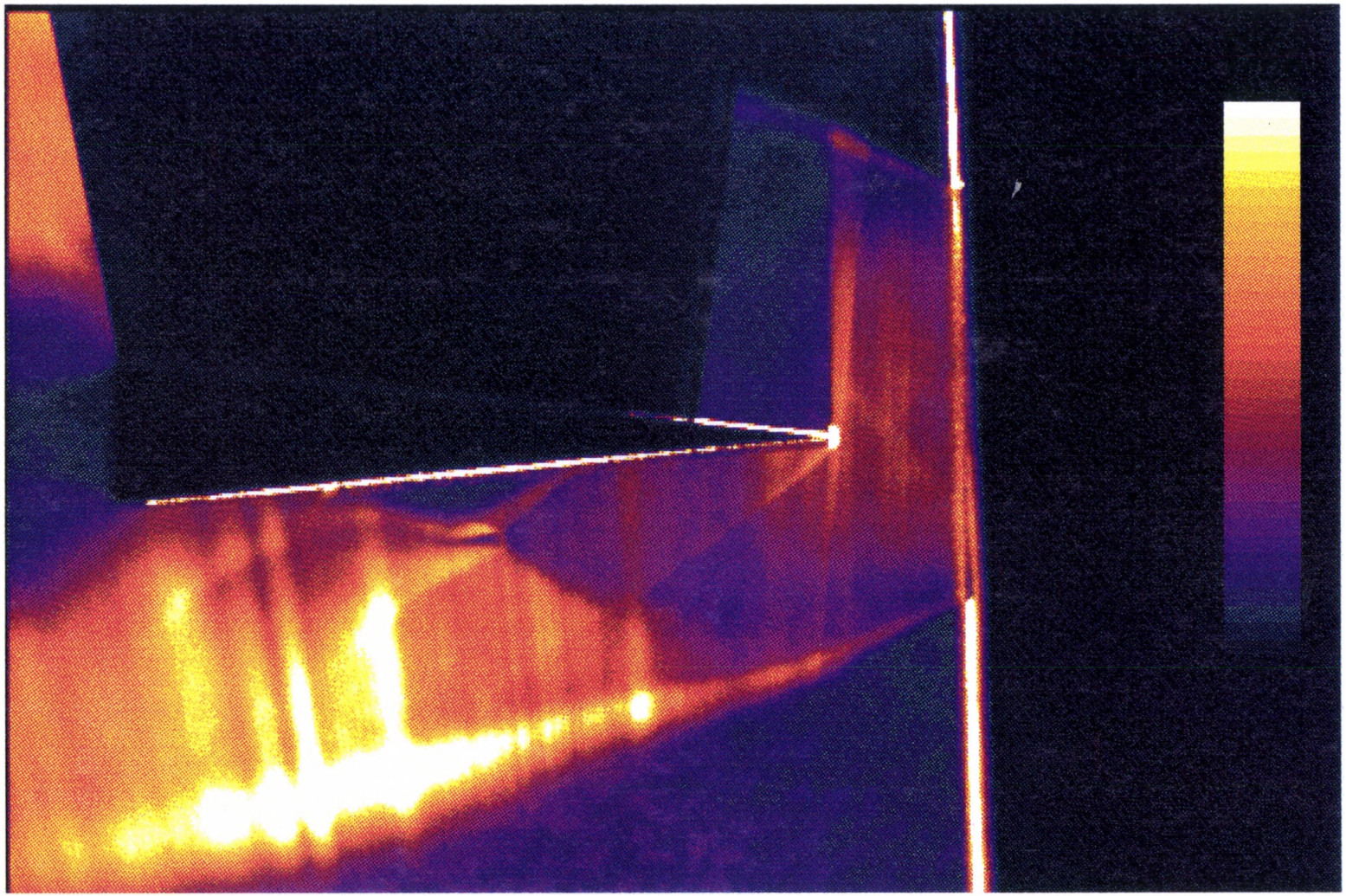

Figure 10: Pseudocolor version of Mach 1.5 image shown in Figure 9. (Scale: 2.15x)

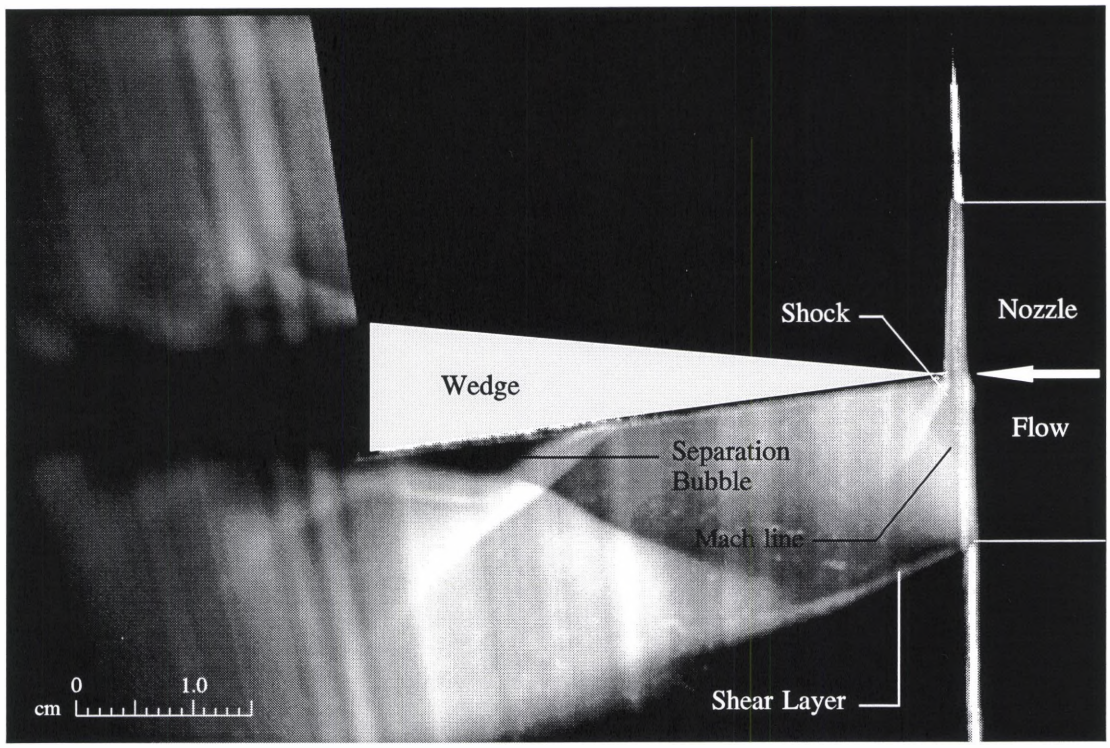

Figure 11: Single-wedge with 5.8° half-angle in a Mach 1.5 flow. Separation is occurring on the rear lower surface. (Scale: 1.54x)

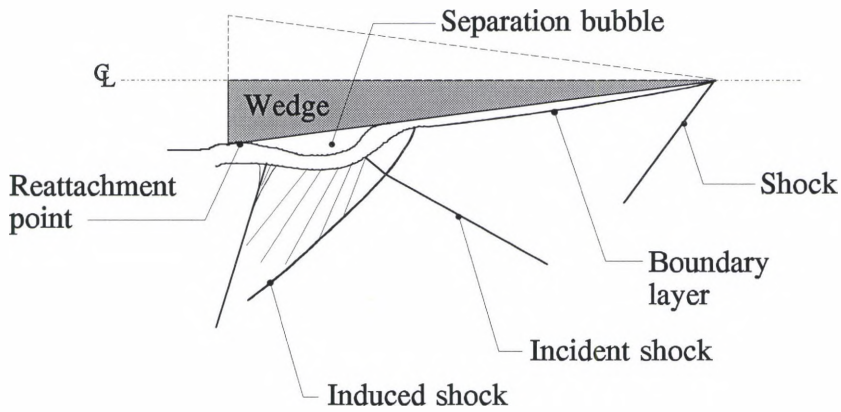

Figure 12: Schematic of a shock wave and boundary layer interaction causing flow separation.

good overview of shock induced boundary layer separation can be found in [16]. The height of the separation bubble is about 0.11 in (2.7 mm). Conditions were such between the incident shock and the induced shock in Figure 9 that a small normal shock was formed. These two waves contribute according to the 'second throat' effect presented earlier.

A final note on Figure 11 is that the angle of the shock on the leading edge indicates a Mach number of 1.27. This is misleading because the leading edge is located inside a zone of underexpansion. Since the flow will continue to expand, the leading edge will be experiencing a higher velocity.

The concluding image in the supersonic series shows the same single-wedge experiencing a Mach 2.0 flow (Figure 13). The wedge was placed 0.21 in (5.4 mm) from the exit of the Mach 2.0 nozzle. To confirm expected features on the upper surface, the laser light sheet, was reflected by a mirror above and out of view of the image. The vertical bright line at the wedge tip is simply an overlapping of the original and reflected light sheet. From the appearance of the shear layer angles the nozzle is experiencing little underexpansion. Likewise there is no existence of weak Mach waves just outside the nozzle exit which would indicate further expansion. Therefore, the calculation of a 1.8 Mach number based on the upper leading edge shock angle of 41° stands within reason. This represents a 90% efficiency relative to the inviscid nozzle design. Similar to the Mach 1.5 case, a shock induced separation bubble exists at the rear of the wedge and contains all of the same feature as discussed above. Recalling the principles of a free jet versus a solid boundary, the lower 'oblique' shock from the leading edge is reflected as an expansion (barely visible) off of the shear layer just below the boundary layer separation. The height of the separation bubble in this image is about 0.016 in (0.4 mm). Based on other images of a wedge in a Mach 2.0 flow, the bubble was consistently very shallow. This suggests a dependence on Mach number, i.e., strength of the flow, and thus incident shock angle. Similarly, the location of occurrence on the wedge was repeatable.

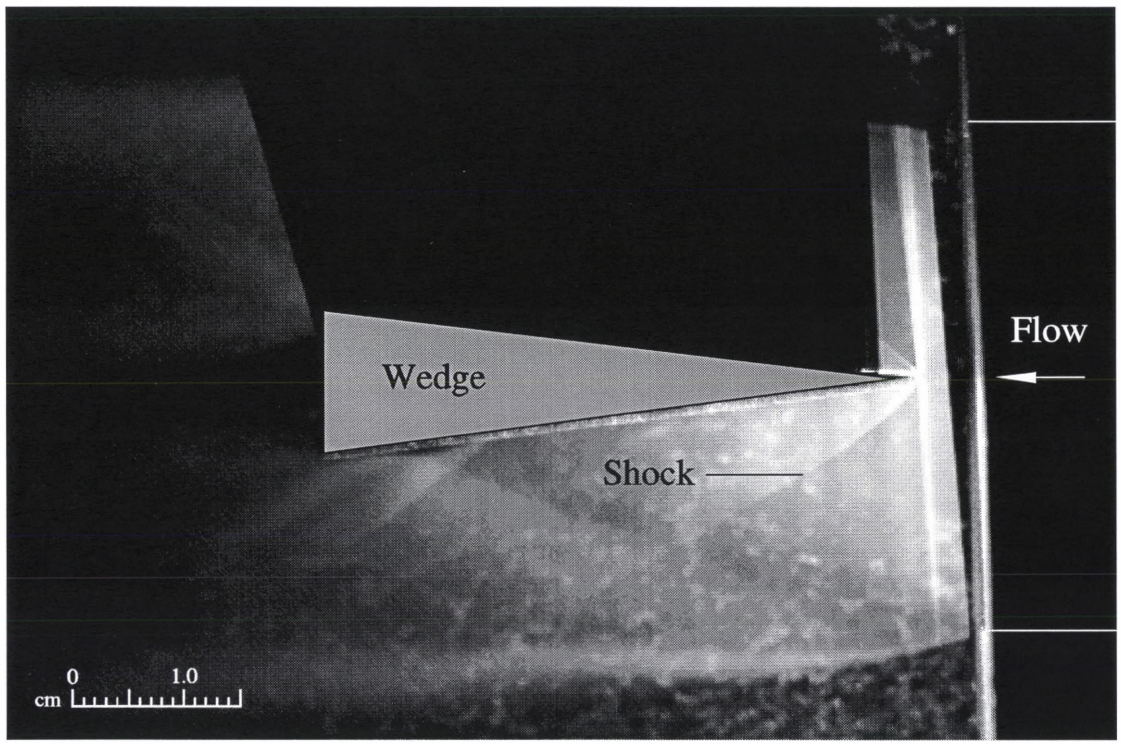

Figure 13: Mach 2.0 flow about a single-wedge with a 5.8° half-angle. (Scale: 1.53x)

CHAPTER

4

PHASE LOCKING APPLICATION

4.1 INTRODUCTION

The second phase in determining suitable flow visualization techniques for the transonic compressor environment involved the ability to capture an image of a rotating blade row. The main task was to periodically deflect a laser beam such that it would strike the blade every cycle. This phase locking was facilitated by using an acousto-optic modulator and its driver to swing the beam from the main path at the frequency of the rotating fan. The success of this process at low speed is assumed to be comparably achieved at frequencies on the order of 20,000 rpm in the transonic case.

4.2 EXPERIMENTAL DETAILS

4.2.1 ACOUSTO-OPTIC MODULATION

The device selected to deflect the laser beam was a NEOS (*Newport Electro-Optics Systems*) acousto-optic modulator (*AOM*). In general, this component allows manipulation of a laser beam from an electrical input signal. Both deflection and modulation of the laser amplitude are possible. Upon receiving the acoustic signal, the optical medium generates a refractive index wave that behaves like a sinusoidal grating. The medium is a tellurium dioxide crystal, which is very commonly used for AOMs. A laser beam

passing through the grating will defract into several orders—each order possessing a decrease in intensity. A linear relationship exists between the diffracted beams angular displacement and the signals acoustic frequency. The intensity of light deflected is a function of a material figure of merit, the acoustic power, geometric factors, and the wavelength (λ) [17]. The AOM used in this study was certified to have an efficiency of 77% at λ=632.8 nm (He-Ne). For diffraction to occur, the Bragg angle between the AOM and the incident laser beam had to be adjusted. A rotary stage was mounted to the bottom of the AOM to facilitate angle adjustment.

To interface the raw signal with the AOM, a NEOS medium power radio frequency generator, known as the AOM driver, was used. This driver received maximum inputs of 15V DC and 1 Amp, respectively, while providing a maximum output power of 1.25 Watts. An input signal was supplied to the AOM driver through the use of pulse generator.

The original sinusoidal signal from a function generator (*FG*) was sent to a pulse generator (*PG*). The FG's external gating signal provided the triggering waveform for the period circuitry within the PG. Features of period, duration, delay and transition time permitted customized control ranges. Generally speaking, the PG outputs a pulse upon the peaking of the sinusoidal signal (positive or negative only). The AOM driver receives the output of the PG and excites the crystal grating of the AOM. An oscilloscope was used to monitor the output for a proper signal.

4.2.2 Light Source and Camera System

The Helium-Neon laser discussed in Section 3.2.4 was also used in the phase locking demonstration for imaging purposes. A similar system will be used in the transonic study. Likewise, the CCD camera used in the supersonic proof-of-concept was employed to test the motion-capturing abilities of rotating hardware. The modulated laser beam was spread into a sheet using a cylindrical lens having a width of 0.748 in (19 mm)

and a radius of 0.984 in (25 mm). The choice of lenses was simply due to the available working area on the optics table. It also provided a 'cleaner' light sheet in the sense of no visible striations and allowed us to view its optical characteristics relative to its dimensions. A series of front-surface mirrors, similar to those discussed in the previous chapter, guided the modulated beam around the table to the rotating fan as shown in Figure 14. The orientation of the light sheet direction is normal to the plane of rotation for this demonstration. It will be of interest in the compressor rotor study to orient the light sheet in such a way as to illuminate the blade-to-blade passage and/or the flow either side of a blade. Therefore, the light sheet will need to be directed at an appropriate angle to the rotation plane due to the twist of the rotor blades.

4.2.3 Rotating Blade Row

Receiving the pulsed laser sheet, was an 18 in (457.2 mm) diameter single blade row. It consisted of six blades mounted to a 4.5 in (114.3 mm) diameter hub. The fan was driven by a Dayton Electric 1 hp (745.7 W) DC motor. The motor's variable speed controls allowed a fan to achieve 2154 rpm (35.9 Hz). The entire fan was commercially fabricated from aluminum and was painted black to provide a uniform dark surface for reflecting the laser sheet and minimizing stray light reflections.

4.3 Data Acquisition and Processing

For the laser beam to be diffracted, the angle had to be adjusted between the AOM and the beam. Since this critical angle had a tolerance of about 1 mrad (3.4 arcmin), a rotary stage was mounted at the base of the AOM. The stage was adjustable with coarse and 80-pitch fine thread screws with a resolution of 0.15 mrads (30 arcsec). With the laser beam launched into the center of the crystal and RF power applied, an array of light spots was emitted from the AOM onto any surface in the beam path. The array consisted

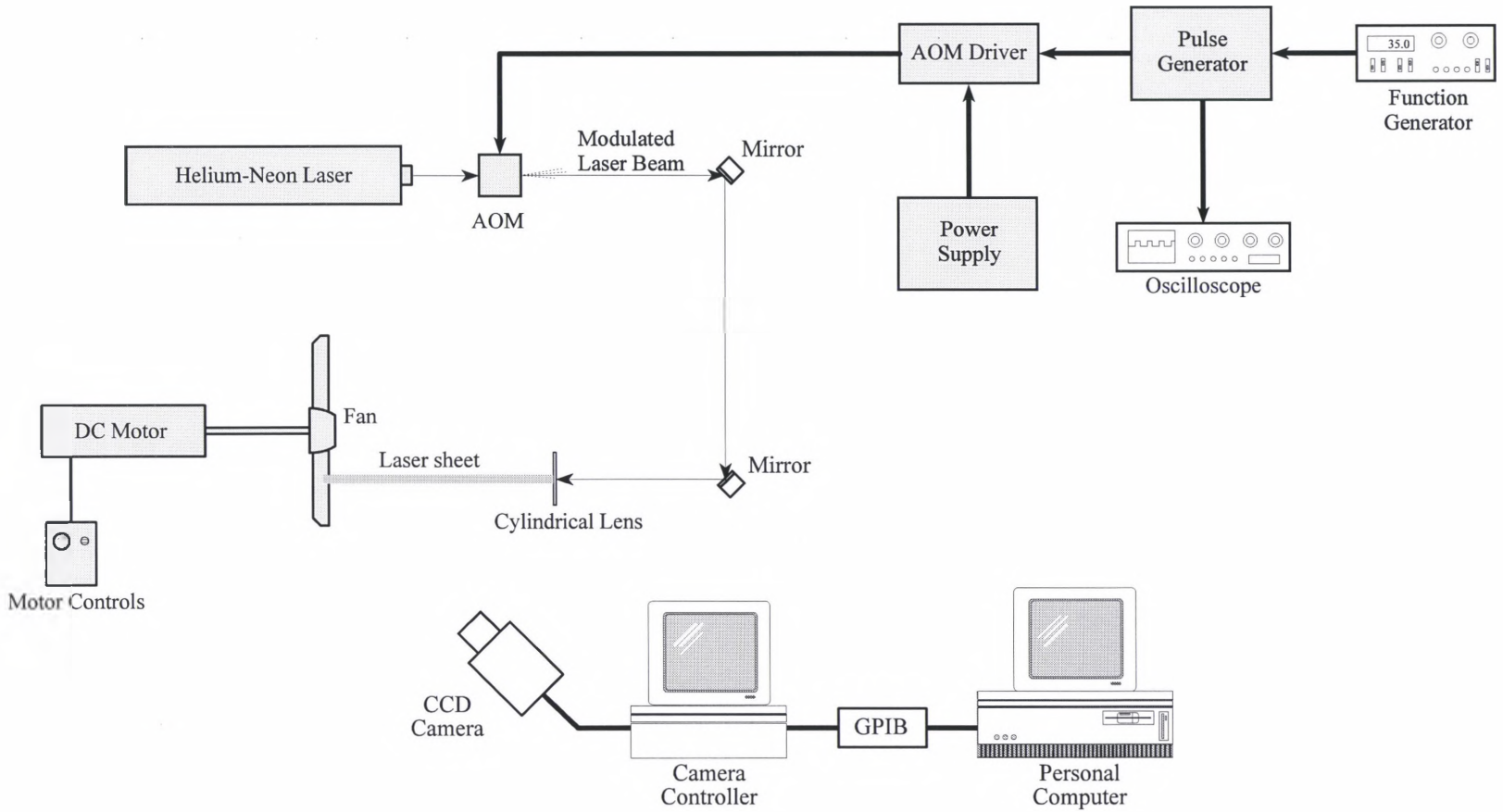

Figure 14: Schematic of phase locking demonstration.

of the main beam and modulated beams diverging either side of it which we shall call ± first order, ± second order, and so on. Usually, up to five or six visible spots were present at one time with the intensity of each beam decreasing counting outward from the center beam. Several iterations of vertical, horizontal and rotational adjustments of the AOM provided an optimum setting of the array. The + first order beam was isolated onto the mirrors since it provided the highest intensity. It was guided around the optics table passing through the cylindrical lens and struck a fan blade. With the fan near peak rotation, as restricted by the motor limits, a strobe light was aimed at the fan to determine its frequency of rotation then turned off. The sinusoidal signal from the FG was set to roughly match the fan frequency. With some tweaking of the FG, a single fan blade was *locked* into position thus eliminating the appearance of precession. Hence, the frequency of the AOM coincided with that of the fan.

This demonstration provided another test of the CCD camera which was used in the supersonic case. Without external triggering utilized, the camera exposure time was set to the minimum of 0.1 s. When the desired modulated conditions were obtained and the phase locking of the fan held, an image was acquired.

4.4 RESULTS

Figure 15 shows the fan with an incident laser sheet striking at about 60% from the blade root. The fan and AOM had a matched frequency of about 36 Hz. An image was acquired of the stationary fan to reveal the geometry of the blade row and can be seen in Figure 15(a). The camera was then used to capture the rotating fan and modulated sheet which are shown in Figure 15(b). Both images were obtained under high fluorescent light levels to clearly indicate the fan orientation, yet not washing out the incident laser. The incident light sheet is distinctly seen as about 2 in (50.8 mm) long but could be adjusted to cover a much larger region. Since only the hub is visible, the

(a)

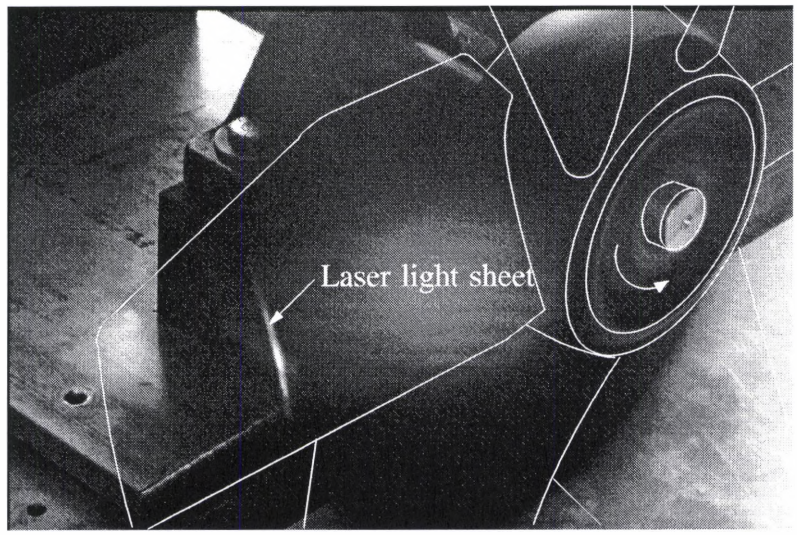

(b)

Figure 15: Laser sheet modulated to frequency of fan. (a) stationary fan showing geometry, (b) fan at 36 Hz with visible light sheet.

blades have been annotated. The exposure time of the camera was set for 0.1 s, therefore the image acquired 3.6 pulses of the modulated sheet. The PG was adjusted for a duration of 0.1 ms, with pulse duration defined as the time interval between the leading and trailing edge of a pulse at which the instantaneous amplitude reaches 50% of the peak pulse amplitude. A moderate transition time between the 10% and 90% amplitude levels was set for 5 μs corresponding to 5% of the pulse duration.

The transonic study involves a transonic compressor rig achieving rotational speeds of up to 21,500 rpm [18]. Since the stand-alone camera system has a lower exposure limit of 0.1 s, a total of 35.8 cycles would occur at maximum speed during that exposure. To facilitate capturing an image with as low as one cycle per exposure, an external trigger mechanism can be used. The camera controller has a port allowing an external trigger signal to be input for a minimum of 20 μs. An integration time will be set on the video display—in this case, 0.1 s. Upon arming the trigger the shutter opens and continuously clears the CCD of charge until the external trigger signal is sent. When the trigger signal is received by the controller, the CCD array ceases to be cleared of charge and receives information for the preset external time. If one cycle of the rotor is desired, an external integration time of 3 ms would be required. This obviously falls within the system's lower limit of 20 μs.

CHAPTER

5

UNSTEADY DEMONSTRATION

5.1 INTRODUCTION

The final major interest of the study surrounds the application of an artificial tracer to the flow visualization process. In the supersonic demonstration, the condensed water vapor made available from ambient conditions served well as the tracer to reveal shock structures. However, in the closed-loop transonic facility, the working pressure of up to two atmospheres will require a tracer to be *seeded* into the flow. An artificial smoke generator was chosen for its ease of use and desirable characteristics of the fluid source. To demonstrate the illumination ability of the smoke, a small model was placed in a low-speed wind tunnel. The unsteady interaction of the smoke, model and laser illumination was captured by the CCD camera used in the previous phases of the study. The model being a circular cylinder normal to the flow provided trailing vortex patterns. The periodic formations were made clearly visible as expected.

5.2 EXPERIMENTAL EQUIPMENT AND FACILITIES

5.2.1 LOW SPEED WIND TUNNEL

One of the wind tunnels at the University of Dayton is a small scale subsonic tunnel used primarily for visualization studies (Figure 16). The open-loop tunnel begins

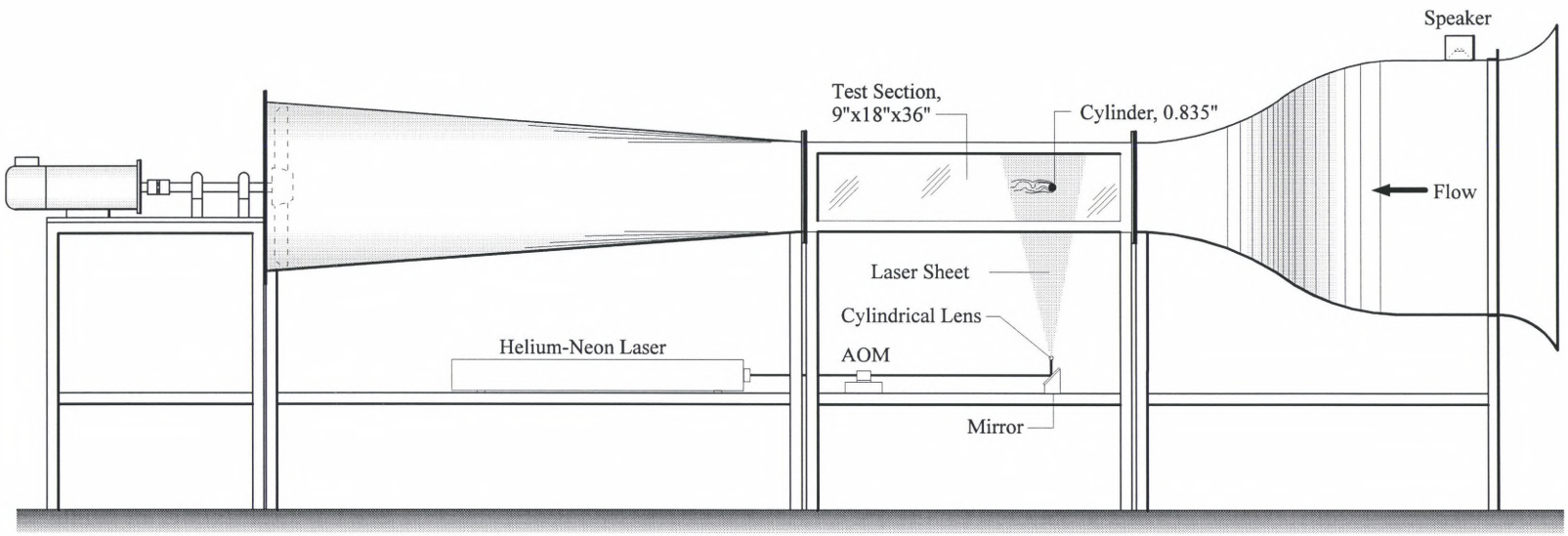

Scale: 1"=1'-9"

Figure 16: Subsonic wind tunnel facility for unsteady flow demonstration.

with an inlet having an area contraction ratio of 10:1 and a series of screens to provide a uniform flow to the test section. The 9 in × 18 in × 36 in (22.86 cm × 45.72 cm × 91.44 cm) test section is equipped with a full acrylic front window and manometer. Additionally, a ¾ in (19.05 mm) longitudinal slot on the test section floor allows instrumentation to access the flow. The 60 in (1.524 m) diffuser gradually expands the flow from the test section exit to a 19 in (48.26 cm) diameter diffuser exit. Driving the flow is the motor and fan unit described in Section 4.2.3, which was removed from the tunnel solely for the phase locking demonstration. The maximum setting on the variable speed controls of the motor produces a flow velocity of about 61 ft/s (18.5 m/s).

5.2.2 Flow Tracer

The seeding of the flow was made possible by a portable fog generator with duct-work connecting it and the tunnel inlet. The generator, which is made by JEM Smoke Machine Co. LTD. in Lincolnshire, England, is the type commonly used for theatrical or concert special effects. The unit measuring roughly 9 in × 9 in × 24 in (22.9 cm × 22.9 cm × 61 cm) is powered by a 1.34 hp (1000 W) heater. The working fluid is siphoned off a removable bottled reservoir and heated to form the fog. After a short warm-up period of about 5 to 10 minutes, the fog is emitted by a high-pressure oscillating pump operating at 65 lb/in^2 (448 kPa). Although the exact make-up of the fluid is proprietary, the general constituents consist of food-grade polyglycols and distilled water. It is a very safe substance to work with: there are no special storage precautions, it is non-flammable, it presents very low toxicity to the environment, and is biodegradable. Noticeable on surfaces after prolonged use was a slight film, but this evaporated after a few days. Since the smoke is emitted from the generator at a high temperature, there is a tendency for it to rise. In a closed-loop environment this is not expected to be a problem due to the high velocity and mixing. For the supersonic case in Chapter 3, the water vapor proved suitable for the results obtained, although it was of interest to integrate the artificial fog

into the flow. The simplest way, would have been to feed the fog into the pressurized tank. Since the pressure limitations on the fluid were not revealed by the manufacturer, the risk of pressurization was not taken for fear of auto-ignition. Another option would have been entraining the fog at the nozzle location, but was not pursued based on the previously acceptable results. As presented later, the simple flow about a model in a wind tunnel provided adequate results for observing the fogs characteristics for laser illumination.

5.2.3 Model

The model was a cast iron right-circular cylinder having an outside diameter of 0.835 in (21.21 mm) and a length:diameter aspect ratio of 21.6. It was mounted to the back wall of the test section with a threaded pipe flange and spanned the entire lateral distance to make contact with the front acrylic window. Since the cylinder was cast iron, it was sanded to remove obvious imperfections and then painted black to minimize glare from the laser sheet. The model was located about 9.5 in (24 cm) from the test section inlet and at the vertical centerline. The blockage of the cylinder with respect to the test section height was 9.3% which is an acceptable value to minimize sidewall interference. Likewise, the cylinder spanned the entire lateral length of 18 in (45.72 cm) to provide a two-dimensional flow for the region of interest.

5.2.4 Acousto-Optic Modulation and Flow Excitation

The setup for the light source and the steering of the laser sheet was similar to that used in the supersonic demonstration with a couple of exceptions (Figure 17). The laser beam was guided around the optics table with mirrors then directed 90° upward to penetrate the glass cylinder as before. Hence, a laser sheet was produced. In the present unsteady application, the AOM, driver, and supporting instruments were integrated into the process to modulate and deflect the beam. The intent was to have the vortex shedding

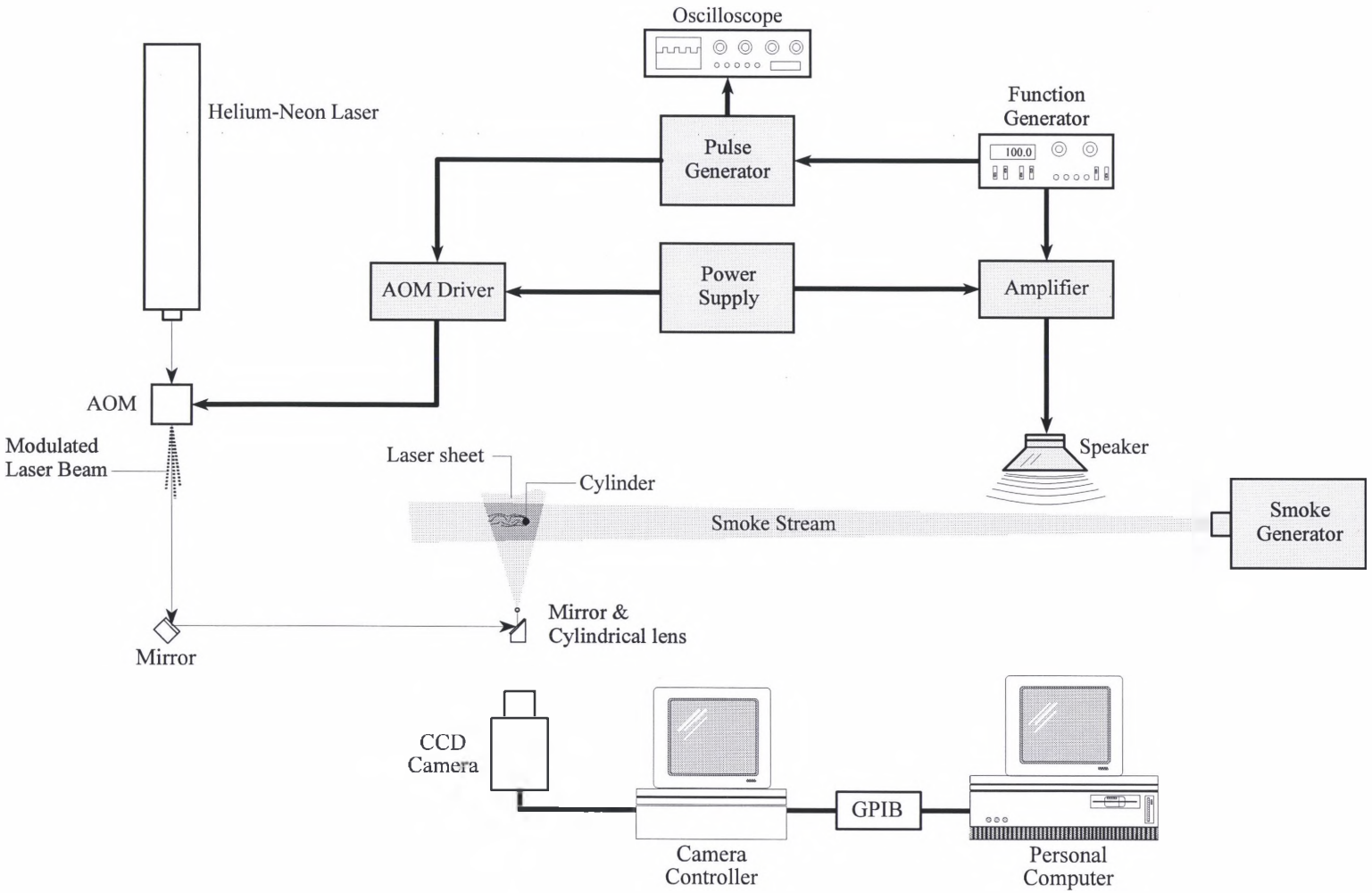

Figure 17: Schematic of unsteady flow demonstration.

frequency of the circular cylinder phase-locked with the acoustic signal.

Artificial excitation has been used by others for the purpose of stabilizing and destabilizing shear flows. Roos and Kegelman [22] suggest that stimulating the flow over a backstep results in alteration of major flow features. They showed that modifications in vortex development and the control of the reattaching flow were possible. An oscillating trailing edge flap at the point of shear layer separation was used to excite the reattaching shear layer. With the use of pulsed laser sheet illumination, photographs revealed that the flap provided a very noticeable 'regularizing' influence on the development of vortex structures downstream. Roos and Kegelman noted that "when excitation is effective in organizing and regularizing development of the large-scale vortical structure in the reattaching shear layer, (the point of reattachment) is almost the same for fully laminar and fully turbulent separations". In both cases, the reattachment length was typically reduced by at least one step height. However, the effect of exciting the flow was not as predictable in the transition range of Reynolds numbers.

An extension of the flow excitation has been treated by many with the active use of feedback control. A good survey of this approach was covered by Roussopoulos [23]. Vortex shedding from a circular cylinder was investigated by the closed-loop control method of sensors, in the form of hot-wires, and actuators, in the form of a speaker and amplifier. The shedding cell growth rates were suppressed at a single spanwise point and in the vicinity of the control sensor with the use of acoustic feedback. This was typically done at Reynolds numbers just above the onset of vortex shedding. Similarly, Monkewitz [24] presented analytically that feedback control could also be used in destabilizing flows. Hussain and Ramjee [25] investigated, among other things, the interaction of the periodic shedding phenomenon with an imposed periodic acoustic disturbance. They pursued the *locked-in* event, as well as the suppression of vortex shedding. They concluded that when the natural shedding frequency was matched with the controlled sinusoidal pulsations there was no effect on the natural frequency. However, as the controlled acoustic signal was

increased above the natural frequency, the pulsations diffused the vortices while the vortex cell spacings were unaffected.

In the present study, a speaker was placed on the top of the inlet to excite the flow, as shown in Figure 16. Prior to reaching the speaker, the sinusoidal signal from the function generator was enhanced by an amplifier. Coupling of the shedding frequency with the signal to the speaker and AOM was done. Although exact matching of the frequencies was not found, *regularization* of the flow was noticeable when matching converged. The Reynolds number of this experiment was much higher than the majority of those in the papers referenced above.

5.3 Data Acquisition and Processing

The imaging procedure began by aligning the laser, AOM, mirrors, and cylindrical lens in such a way as to illuminate the cylinder and a region downstream where vortical structures were expected to occur. The AOM was painstakingly adjusted by the steps outlined in Section 4.3. To phase-lock the AOM with the shedding frequency, a wind tunnel setting was first chosen, and the corresponding flow velocity was noted. With the velocity, cylinder diameter, and a Strouhal number based on the Reynolds number as knowns the shedding frequency was the only unknown. This was used as the input to the function generator which was subsequently conveyed to the AOM. The camera was positioned on a tripod with the camera centerline normal to the test section window at a distance of about 24 in (61 cm). With a steady flow and the camera system readied, the smoke generator was remotely activated to emit a short burst of fog. As the smoke became visible in the flow local to the cylinder, the camera shutter was triggered for an exposure time of 0.1 s. Several attempts were usually required, due to extraneous smoke obscuring of the field of view. It became obvious, that the control of the tracer, in terms of providing uniformity with appropriate ducting, would be a consistent problem. The

imaging process was done with all local facility lighting turned off, thus allowing only the laser to illuminate the flow.

5.4 RESULTS

An image of the 0.835 in (21.21 mm) diameter cylinder generating vortical structures is shown in Figure 18. For the circular cylinder, this suggested a Reynolds number (*Re*) of 11,500. A Strouhal number was calculated from $S=nD/V$, where n is the vortex shedding frequency of the cylinder, D is the diameter and V is the freestream velocity. A moderate wind tunnel setting provided a flow velocity of 27.8 ft/s (8.5 m/s). Using S=0.20, which is based on measurements performed by Roshko [19] and a function of Reynolds number, it was determined that $n\approx$80 Hz. [*The Strouhal number was initially calculated to be about 100 but was based on an incorrect value for density in determining the flow velocity. A recheck of the value of S prior to the generation of this paper exposed the error*]. A sinusoidal signal of 100 Hz (of course, based on the calculation error) was input to the function generator.

The tracer was fed into the tunnel inlet with flexible PVC ductwork. A flexible aluminum fitting on the end of the duct was shaped to form a vertical sheet of smoke. The smoke sheet was directed such that it sliced the cylinder midspan to coincide with the incoming laser sheet.

The cylinder in Figure 18 is very close to full scale in the image, but appears fuzzy on the perimeter due to the cylinder end being 8 in (20 cm) closer to the camera than the Kármán vortex street [20]. In a case such as this, scaling determination should be made referencing, say, the cylinder shadow although difficult in this image. For a Reynolds number less than $\sim 10^5$, one would expect a laminar boundary to exist with separation to occur near the upper and lower surface of the cylinder. This is evident in the image if one extrapolates the lower portion of the smoke stream back to the obscured

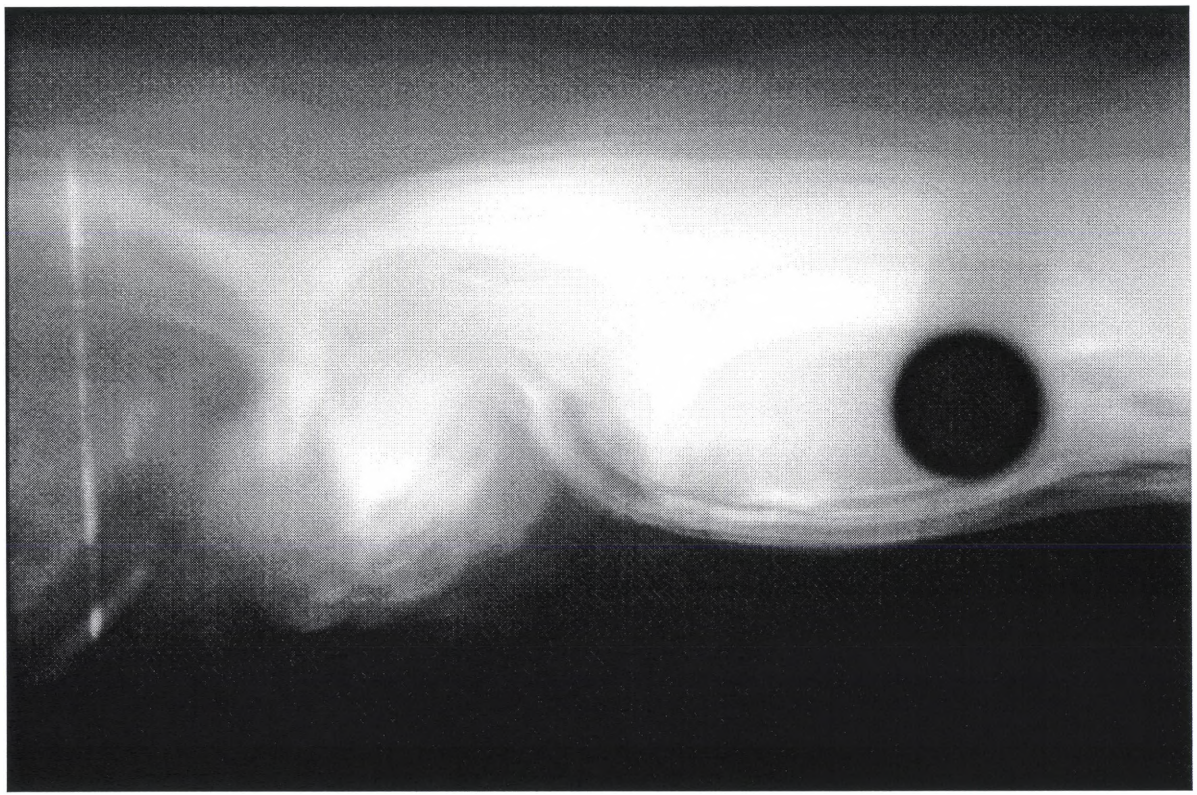

Figure 18: Vortex formations behind a 0.835 in (21.2 mm) diameter circular cylinder. Re = 11,500; (Scale: 0.96x)

outer region of the cylinder. Downstream of the cylinder, there is evidence of four vortex formations. The most recent vortex is one moving counterclockwise from the top of the cylinder but preceded in time by a pattern of three alternating vortices. The reader is referred to Schlichting for a good explanation of the mechanisms behind boundary layer separation of a cylinder [21]. Essentially, the kinetic energy of the boundary layer is diminished by viscous interaction with the cylinder surface. There is a point along the surface such that there is no longer enough kinetic energy to overcome the pressure gradient and remain attached. A reversing motion of the fluid occurs between this point and the rear of the cylinder. The reversal of flow interacting with the oncoming flow results in the onset of a vortex. As the most recent vortex begins to *break away* from the cylinder, the pressure conditions are such that another is allowed to form on the opposite side and in the opposite direction of rotation.

Due to the small dynamic range of the digital image, enhancing the image to reveal better detail was difficult to achieve. It was of interest to see if more detail could be brought out by using the *IMAGE* program introduced in Chapter 3. Again, 32 levels of pseudocolor were applied and the result is shown in Figure 19. The four vortex structures and laminar boundary layer are more distinct. The scale representing the 32 colors is located in the lower right hand corner. Recall that caution should be taken when viewing the image regarding nonuniformity of the light sheet intensity.

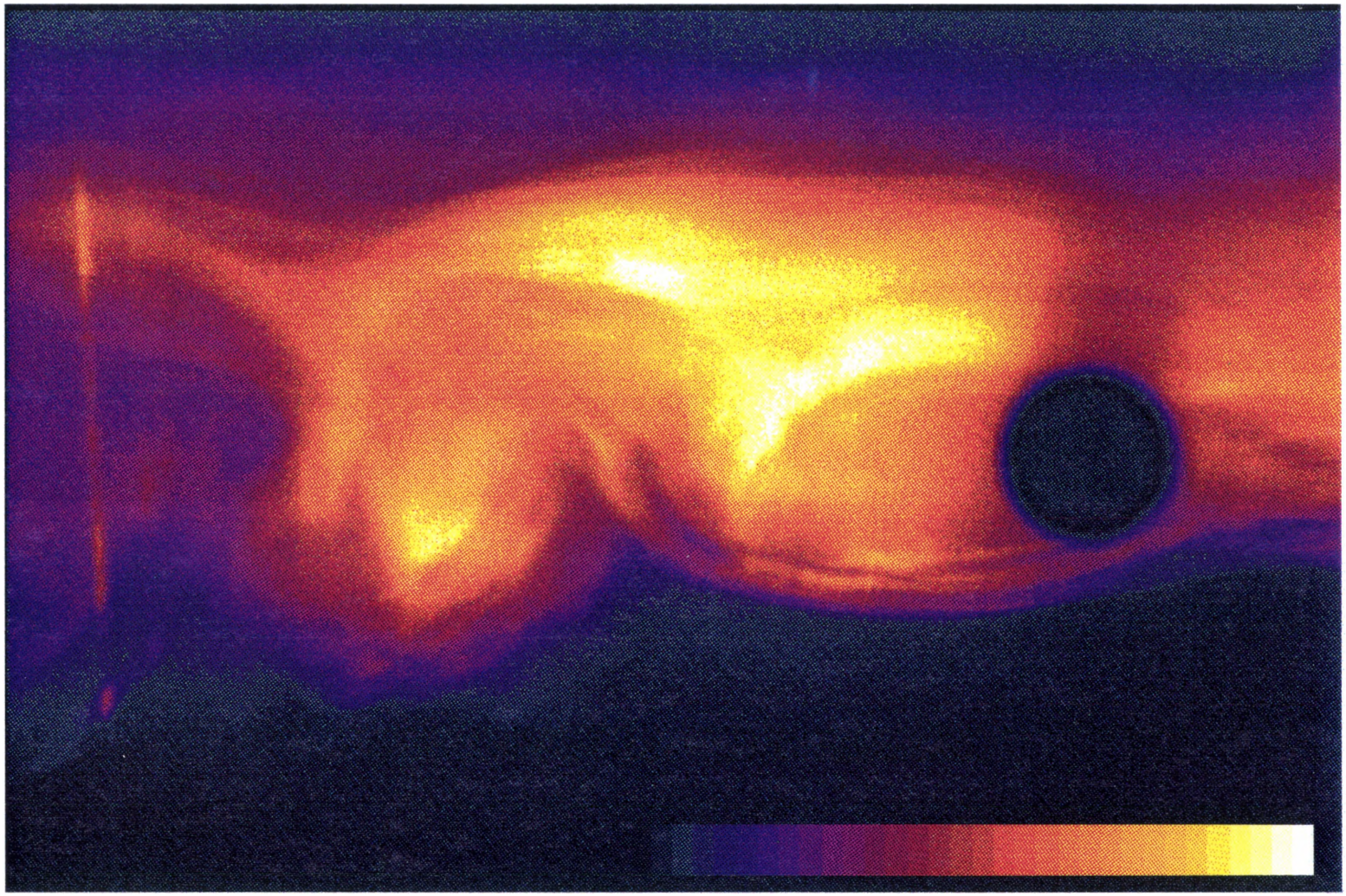

Figure 19: Pseudocolor version of image shown in Figure 18. Cylinder dia. = 0.835 in (21.2 mm). Re = 11,500; (Scale: 1.39x)

CONCLUSION

A study has been undertaken to examine the problem of recording the flow structures in transonic compressor rotor. The technique of imaging the flow structures with a CCD digital camera has been successfully demonstrated. The application of a *vapour-screen*, as used by McGregor, was extended here to be integrated with the digital camera. Images acquired in a supersonic flow clearly indicate flow structures such as bow and oblique shocks, expansion regions, and boundary layer-shock interactions. This was done simply by using the available water vapor in the surroundings. For use in the transonic facility, the laser sheet and CCD camera will be used to image flow structures in the blade passages. It is likely, that an artificially injected tracer will be necessary to assist in illuminating the activity. Further studies on the thermodynamic properties of the tracer will be required. The difficult timing methodology involved in the high-speed transonic facility is believed to be overcome by the remote triggering ability of the digital camera. A technique to insert a laser sheet with an optical probe downstream of the compressor rotor is being investigated and appears promising.

A summary of desirable features of the techniques presented in this paper are:

- Relatively low cost digital camera with simple setup and operation.
- Camera usable in very low light levels–from common light to laser beams.

- Resulting images can be viewed immediately after exposure.
- Subtle flow structures are ascertainable.
- Images saved to permanent storage.
- First generation hard copy is repeatable.
- Images can be enhanced if necessary.
- Camera shutter can be matched with independently modulated light source.
- External triggering of camera allows a minimum of 20μs exposure.
- Proven applicable to subsonic, transonic and supersonic flows.
- For supersonic flows, ambient water vapor is sufficient for flow tracer.
- For other flows, an artificial tracer can provide additional seeding.

REFERENCES

1. Wood, J. R., A. J. Strazisar, and P. S. Simonyi: (1987) Shock Structures Measured in a Transonic Fan Using Laser Anemometry, *AGARD Transonic and Supersonic Phenomena in Turbomachines*, AGARD-CP-401, pp. 2.1-2.14.

2. Strazisar, A. J.: (1985) Investigation of Flow Phenomena in a Transonic Fan Rotor Using Laser Anemometry, *ASME Journal of Engineering for Gas Turbines and Power*, Vol. 107, pp. 427-435.

3. Allen, M. G., S. J. Davis, and L. G. Piper: (1989) Wind Tunnel Diagnostics Based on Laser-Induced Fluorescence, ISA paper no. 89-0007.

4. Epstein, A. H.: (1977) Quantitative Density Visualization in a Transonic Compressor Rotor, Transactions of the ASME, *Journal of Engineering for Power*, Vol. 91, pp. 460-475.

5. McGregor, I.: (1961) The Vapour-Screen Method of Flow Visualization, *J. Fluid Mechanics*, Vol. 11.

6. Atti del V Convegno Volta: (1935) Reale Accademia D'Italia, Rome, 2nd Ed., 1940.

7. Wegener, P. P. and L. M. Mack: (1958) Condensation in Supersonic and Hypersonic Wind Tunnels, *Advances in Applied Mechanics,* Vol. V, Academic Press.

8. Eber, G. and K. H. Gruenewald: (1941/42) Schlieren-Photography of Condensation Disturbances in the 40×40 cm Peenemünde Supersonic Wind Tunnels. Private communication between Messrs Wegener, Mack, Eber, and Gruenewald.

9. Wegener, P. P.: (1969) Gasdynamics of Expansion Flows with Condensation, and Homogeneous Nucleation of Water Vapor, *Nonequilibrium Flows*, Ch. 4, Pt. 1, Marcel Dekker, New York.

10. Campbell, James F., Joseph R. Chambers, and Christopher L. Rumsey: (1989) Observation of Airplane Flowfields by Natural Condensation Effects, *J. Aircraft*, Vol. 26, No. 7.

11. Brendel, Michael: (1992) Transonic Flow Visualization Using Condensed Water Vapor, Final Report F33615-90-C-2086.

12. Pope, Alan and Kennith L. Goin: (1965) *High-Speed Wind Tunnel Testing*, John Wiley & Sons, New York.

13. Brendel, Michael: (1992) Computer program for viewing, analyzing, and plotting TIFF files., University of Dayton, Ohio.

14. Anderson, John D., Jr.: (1990) *Modern Compressible Flow: with Historical Perspective*, McGraw-Hill Book Co., New York.

15. Rasband, Wayne: (ca. 1992) *Image v.1.43,* a digital image processing and analysis program, National Institute of Health.

16. Anderson, John D., Jr.: (1989) *Hypersonic and High Temperature Gas Dynamics*, McGraw-Hill Book Co., New York.

17. Young, Eddie H.: (1990) "New Materials and Designs are Improving AO Devices", *Laser Focus World*, PennWell Publishing Co.

18. Cheatham, J. G.: (1987) Parametric Blade Study, FR-19425

19. Roshko, A.: (1954) On the Development of Turbulent Wakes From Vortex Streets, NACA Report 1191.

20. von Kármán, Theodore: (1911) Über den Mechanismus des Widerstandes, den ein bewegter Körper in einer Flüssigkeit erzeugt. Nachr. Ges. Wiss. Göttingen, Math. Phys. Klasse pp. 509-517 *and* (1912) pp. 547-556.

21. Schlichting, Hermann: (1979) *Boundary-Layer Theory*, McGraw-Hill Book Co., New York.

22. Roos, Frederick W. and Jerome T. Kegelman: (1986) Control of Coherent Structures in Reattaching Laminar and Turbulent Shear Layers, *AIAA J.*, Vol. 24, No. 12.

23. Roussopoulos, Kimon: (1993) Feedback Control of Vortex Shedding at Low Reynolds Numbers, *J. Fluid Mech.*, Vol. 248.

24. Monkewitz, P. A.: (1989) Feedback Control of Global Oscillations in Fluid Systems, *AIAA Paper* 89-0991.

25. Hussain, A. K. M. F. and V. Ramjee: (1976) Periodic Wake Behind a Circular Cylinder at Low Reynolds Numbers, *Aeronautical Quarterly*, May

VITA

David Bell is a graduate student at the University of Dayton in the Mechanical & Aerospace Engineering Department and will graduate December 1993. Prior to attending UD, he obtained his bachelors degree in Aerospace Engineering at the Florida Institute of Technology in 1992. There he developed a passion for flying and went on to obtain flight training from the F.I.T. School of Aeronautics. As an undergraduate he developed a relationship with Dr. Mike Brendel at F.I.T., later meeting up with him again at UD. David has acquired a background in wind tunnel experience covering subsonic, transonic, and supersonic flows. Although his academics contained a concentration of fluid dynamics, David's immediate goal is to work with wind tunnel testing or in the flight test engineering field. Other achievements include obtaining an A.S. degree from Tampa's Hillsborough Community College in Architectural/Engineering Technology (1983) and presenting a paper at the 1993 AIAA Dayton-Cincinnati Section Mini-Symposium. While living in Tampa and Orlando for 28 years, David met his wife Karen and married in 1989. David will be employed by the Boeing Commercial Airplane Group in Seattle, WA.